Master's thesis

NTNU
Norwegian University of Science and Technology
Faculty of Engineering
Department of Marine Technology

Herman Schrader Bordal

Estimation of Higher Order Wave Loads on Offshore Monopiles

Master's thesis in MTMART
Supervisor: Trygve Kristiansen
June 2020

NTNU
Norwegian University of
Science and Technology

Herman Schrader Bordal

Estimation of Higher Order Wave Loads on Offshore Monopiles

Master's thesis in MTMART
Supervisor: Trygve Kristiansen
June 2020

Norwegian University of Science and Technology
Faculty of Engineering
Department of Marine Technology

NTNU
Kunnskap for en bedre verden

Abstract

Kristiansen and Faltinsen (2017a) showed that the inviscid FNV theory over-predicts the third harmonic wave load on bottom fixed vertical surface-piercing cylinders for long and steep waves. The analytic solution is obtained by potential theory, which do not capture flow separation. The KC number in severe sea states indicate flow separation and viscous effects affecting the forces. The need for viscous modelling was apparent to improve existing theories. A combined viscous CFD-FNV method was derived by substituting the 2D inline force from uniform potential theory with viscous 2D CFD.

As experiments indicate 3D effects might have an impact on higher order. A 3D extension to original 2D CFD was included. The term is derived by expanding the CFD results with the remaining terms in the Navier Stokes equation, and assuming that the slender body assumption is valid. The CFD-FNV theory did improve the estimation on third harmonic loads compared to the FNV theory with fifth order stokes wave kinematics. Forces were accurately estimated for a broad range of wave conditions. The discrepancy between the inviscid FNV theory and experiments were, partially, corrected by the combination of viscous CFD analysis and the inclusion of the newly derivated slender body term.

The experiments by Kristiansen and Faltinsen (2017a) were reconducted to get visual data of possible 3D effects. A narrow run-up at the rear of the cylinder in regular waves was observed, the phenomenon has previously been mentioned in several papers. The observation lead to an investigation of methods to describe the phenomenon, and subsequently involve the effect in the analysis. This unfortunately came to a halt as the project was limited by time. This is thus left for further investigation.

Contents

Nomenclature

Numerics

δ_{ij}	Kronecker delta
ϵ	Perturbation parameter
$\frac{\partial}{\partial}$	Partial differentiation
$\mathbf{n}$	Normal vector
μ	Dynamic viscocity
∇	Nabla operator
ν	Kinematic viscocity
Σ	Sum
Co	Courantnumber
y^+	Dimensionless wall distance

Abbreviations

CFD	Computational Fluid Dynamics
FNV	Faltinsen, Newman, Vinje

Main Symbols

λ	Wave length
$\mathbf{f}$	Body force
$\mathbf{V}, \mathbf{U}$	Velocity vector
ϕ	Velocity potential

ψ	Higher order diffraction potential
ρ	Density
ζ	Wave Amplitude
a	Radius
a_{ij}	Added mass coefficient
c_ω	Wave celerity
C_D	Drag coefficient
C_M	Mass coefficient
D	Diameter
F	Force
g	Gravitational acceleration
H	Wave height
h	Water depth
k	Wave number
m	Mass
p, P	Pressure
T	Periode
t	Time
u_i	Velocity in i direction

Chapter 1

Introduction

1.1 Motivation

The worlds energy demand is rapidly increasing, all while traditional fossile fuel is being phased out. This leads to increased pressure on environmentally friendly solutions. In order to fulfil the energy demand, the wind industry is expanding their domain offshore, creating a fast growing marine sector. The most common offshore wind turbines today are bottom fixed structures. Technology for these, still need improvement to create a more cost efficient design in order to be competitive with fossile fuel energy production.
Bottom fixed monopile design wind turbine towers have a natural periode of roughly four to five seconds. This unfortunately coincide with the 3ω components of the incoming waves in severe wave conditions. A severe sea condition, ultimate limit state condition (ULS), at the location of offshore monopile typically has 10 to 15 seconds peak periode. Therefore it is crucial to accurately model these higher order excitation load components, which excite resonance.

1.2 Background

Experiments have shown that offshore wind turbines are prone to be excited by transient ringing loads. Ringing is defined as the transient vibrational response occurring after a high steep wave at higher frequency than the incident waves. The observed behaviour can not be explained by traditional wave diffraction theories such as Maccamy and Fuchs (1954). During the first years of 1990s multiple authors tried to derive a method for calculations the excitation loads. The effort culminated in a few potential theory theories for estimation of such loads. Malenica and Molin (1995a) derived a third order diffraction theory using a standard perturbation series. In contrast to Malenica and Molin (1995a) did Faltinsen et al. (1995) allow the wave height to be of the same order as the cylinder radius in his derivation of the forces. Faltinsen et al. (1995) used perturbation theory to include third order wave theory in. The analytic expression, hereinafter referred to as the FNV theory, was generalised by Kristiansen and Faltinsen (2017a) to finite water depth and fifth order waves. As potential theory was assumed for both theories, a limit on the

validity is introduced, due to the occurrence of flow separation at higher KC numbers. The theories have shown to over-predict the third harmonic load by a significant amount in severe sea states. The flow field behind a body in water is impacted by the effect of viscosity and turbulence through the boundary layer. The flow pattern becomes inherently complex if the oscillatory fluid is investigated, where vortices and the high degree of disturbance and turbulence level is brought back to the cylinder surface. The need for viscous modelling is apparent to further evolve, and improve existing theories. The lack of knowledge regarding the viscous effects were mentioned by Kristiansen and Faltinsen (2017a).

1.3 Scope

The scope of this thesis is to examine the effect of flow separation with regards to the third harmonic load on monopiles to create a better load prediction. Viscous effects are to be accounted for by using 2D CFD analysis and assuming that the cross flow principle is valid. The CFD extension is to be included in the FNV theory for a CFD-FNV theory. Additionally an expansion to 2D CFD solution by the use of the Navier Stokes Equations and slender body assumption should be derived, in order to capture 3D effects without using computational heavy 3D CFD analysis.

1.4 Report structure

This report will first present background theory, which is necessary to get the theoretical insight required to both use and extend existing theories. Expansion and continuation of previous work is then presented.
Results of experiments conducted will be presented, with a discussion on phenomenons observed, and the numerical model created in order to recreate the experiments with CFD analysis will be presented. The choice of mesh, solvers and schemes will be discussed. Validation of the method against experiments follows.
The combined CFD-FNV was applied to a monopile with fifth-order wave theory. And the results are presented with a discussion on accuracy, especially regarding the higher order loads. Lastly, a conclusion and recommendations for further works are presented.

Chapter 2

Theory

This section gives insight in background theory and assumptions.

2.1 Fundamental Equations

The governing equations regarding fluid flow is based on three universal conservation laws:

- Conservation of mass
- Conservation of momentum
- Conservation of energy

Conservation of energy is based on the first law of thermodynamics, as heat transfer is neglected this will not be a topic for further discussion.

2.1.1 Continuity Equation

When applying the conservation of mass principle on a fluid we, obtain the continuity equation. Assume the fluid is passing through an infinitesimal control volume, which is fixed in space. Conservation of the fluid mass then yields:

$$\frac{\partial \rho}{\partial t} + \nabla \cdot (\rho \mathbf{V}) = 0 \tag{2.1.1}$$

The rate of change of fluid density is included in the first term, whereas mass flux through the control volume is included in the second term. Rewrite Equation 2.1.1 to the form:

$$\frac{D\rho}{Dt} + \rho(\nabla \cdot V) = 0 \tag{2.1.2}$$

Water is assumed to be incompressible, yielding:

$$\frac{D\rho}{Dt} = 0 \tag{2.1.3}$$

and one obtain the following relation:

$$\nabla \cdot \mathbf{V} = 0 \tag{2.1.4}$$

2.1.2 Momentum Equation

Newton's second law is in fluid dynamics refereed to as the Conservation of Momentum. By recalling the control volume, assuming incompressible fluid and applying Newton's second law, one obtains:

$$\rho \frac{DV}{Dt} = \rho \mathbf{f} + \nabla \cdot \Pi_{ij} \tag{2.1.5}$$

This equation can be recognised as Newton's second law on the form:

$$ma = \sum F \tag{2.1.6}$$

Where the first force term is the body forces acting, such as gravity. And the second term represents the surface forces.

By the Newtonian fluid assumption where the relationship between shear stress and shear rate is directly proportional, Schlisting (1968) derived a deformation law for Π_{ij}. By substituting the equation into the momentum equation (Equation 2.1.5) one obtains the Navier Stokes equation on the following form:

$$\rho \frac{D\mathbf{V}}{Dt} = \rho \mathbf{f} - \nabla p + \frac{\partial}{\partial x_j} \left[\mu \left(\frac{\partial u_i}{\partial x_j} + \frac{\partial u_j}{\partial x_i} \right) - \frac{2}{3} \delta_{ij} \mu \frac{\partial u_k}{\partial x_k} \right] \tag{2.1.7}$$

where δ_{ij} is the Kronecker delta function, and u_i,u_j represents velocities. If we assume the the flow is incompressible and constant viscosity, we can further simplify to:

$$\rho \frac{D\mathbf{V}}{Dt} = \rho \mathbf{f} - \nabla p + \mu \nabla^2 \mathbf{V} \tag{2.1.8}$$

Which we will refer to as the Navier Stokes Equation.

2.2 Potential flow theory

For a broad range of applications, seawater has the properties of a perfect fluid. The fluid is in general considered as incompressible, which is a good approximation of the physical properties. For an external and free flow, the inviscid and irrotational approximation is accurate. Viscosity mostly act in the boundary layer around an object. Potential theory is thus applicable in cases like undisturbed waves. The assumptions for potential theory:

- Incompressible
- Inviscid
- Irrotational

When potential theory is applicable, there exists a velocity potential (ϕ) to describe the fluid motion. The potential ϕ is described as:

$$\mathbf{V} = \nabla\phi \tag{2.2.1}$$

Incompressible flow has zero divergence:

$$\nabla \cdot \mathbf{V} = 0 \tag{2.2.2}$$

One thus obtain the Laplace equation which must hold throughout the fluid.

$$\nabla^2\phi = 0 \tag{2.2.3}$$

(Faltinsen, 1990a)

2.2.1 Boundary Value Problem

To derive a velocity potential for a flow, one needs to define a set of boundary conditions. In the marine environment one often investigates a finite domain with an inlet, outlet, a free surface with air interaction and an impermeable seabed. The domain often contains a body, whose excitation and reaction forces are to be investigated.

2.2.1.1 Boundary Condition at the Seafloor

To enforce the impermeability of a body, the velocity potential needs to satisfy the following equation:

$$\frac{\partial\phi}{\partial n} = \mathbf{U} \cdot \mathbf{n} \tag{2.2.4}$$

where $\mathbf{U}$ is the body velocity and $\mathbf{n}$ the normal vector. At the horisontal seafloor, Equation 2.2.4 simplifies to

$$\frac{\partial\phi}{\partial z} = 0 \tag{2.2.5}$$

as no fluid particles are crossing the seabed.

2.2.1.2 Free Surface

2.2.1.2.1 Kinematic Boundary Condition

> "A fluid particle on the free-surface is assumed to stay on the free surface (Faltinsen, 1990b)."

The free surface can be expressed as:

$$\frac{\partial\zeta}{\partial t} + \frac{\partial\phi}{\partial x}\frac{\partial\zeta}{\partial x} + \frac{\partial\phi}{\partial y}\frac{\partial\zeta}{\partial y} - \frac{\partial\phi}{\partial z} = 0 \quad \text{on} \quad z = \zeta(x, y, t) \tag{2.2.6}$$

2.2.1.2.2 Dynamic Free Surface Condition

Pressure is a continuous quantity, and at the surface the pressure equals the atmospheric pressure. By applying the Bernoulli equation at the surface and enforcing atmospheric pressure one obtain the following boundary condition:

$$g\zeta + \frac{\partial \phi}{\partial t} + \frac{1}{2}\left(\left(\frac{\partial \phi}{\partial x}\right)^2 + \left(\frac{\partial \phi}{\partial y}\right)^2 + \left(\frac{\partial \phi}{\partial z}\right)^2\right) = 0 \quad \text{at} \quad z = \zeta(x, y, t) \tag{2.2.7}$$

2.2.1.2.3 Combined Free Surface Condition

By combining Equation 2.2.7 and Equation 2.2.6 we obtain the free surface condition.

$$\frac{\partial^2 \phi}{\partial t^2} + g\frac{\partial \zeta}{\partial z} + 2\nabla\phi \cdot \nabla\frac{\partial \phi}{\partial t} + \frac{1}{2}\nabla\phi\nabla|\nabla\phi|^2 = 0 \tag{2.2.8}$$

For waves where the wave height is short compared to the length, a linearised, also referred to as airy wave, theory achieve reliable and accurate results. The airy wave theory is obtained by linearising the Taylor expansion of Equation 2.2.8 around the mean free surface. The airy waves approximation yield adequate results over a broad range of problems. However, as sea state severeness increases, the higher order terms is necessary to obtain an accurate solution.

2.2.2 Stokes Wave Theory

Stokes Wave Theory approximates the boundary value problem by a perturbation series approach. These series are dependent on a perturbation parameter ϵ ($\epsilon \sim k\zeta_1$). The velocity potential (ϕ) and surface elevation (ζ) can then be expressed as a series expansion.

$$\phi = \epsilon\phi_1 + \epsilon^2\phi_2 + \epsilon^3\phi_3 + \dots \tag{2.2.9}$$

$$\zeta = \epsilon\zeta_1 + \epsilon^2\zeta_2 + \epsilon^3\zeta_3 + \dots \tag{2.2.10}$$

Similar expressions exist for all variables.
For Stokes theory of nth order, substitute n terms of Equation 2.2.9 and Equation 2.2.10 into the Laplace equation and the boundary conditions. As the combined free surface boundary condition, earlier derived, is evaluated at the free surface, which still is unknown, the equations are Taylor expanded about z=0.

2.2.2.1 Stokes Fifth Order Waves

The accuracy of Stokes Wave theory improves with the inclusion of additional terms. The extent and computational cost of the calculation increases dramatically as terms are added. Skjelberia and Hendrickson (1960) derived a fifth order theory published in 1960. Assuming that both ϕ and ζ are described as trigonometric series. They proposed the following expression:
(The denotation is taken from Skjelberia and Hendrickson (1960) and Brorsen (2007))

$$\phi = \frac{c_\omega}{k}\sum_{n=1}^{5} D_n \cosh(nk(h+z))\sin(n(kx - \omega t)) \tag{2.2.11}$$

$$\zeta = \frac{1}{k}\sum_{n=1}^{5} E_n \cosh(n\theta) \tag{2.2.12}$$

where the wave celerity (c_ω) is given by:

$$c_\omega = \frac{\sqrt{C_0^2\left(1+\lambda^2 C_1+\lambda^4 C_2\right)}}{k} \tag{2.2.13}$$

The quantities E_n and D_n are expressions containing wave length and coefficients dependent on water depth to wave length ratio. The expression for obtaining the coefficients A_{ij},B_{ij} and C_i are given in Skjelbreia and Hendricksons' paper (Skjelberia and Hendrickson, 1960). Fenton John D. (1985) noted that C2 in Skjelbreias paper was denoted with a wrong sign, this is thus changed to be consistent with Fenton John D. (1985).

n	D_n	E_n
1	$\lambda A_{11}+\lambda^3 A_{13}+\lambda^5 A_{15}$	λ
2	$\lambda^2 A_{22}+\lambda^4 A_{24}$	$\lambda^2 B_{22}+\lambda^4 B_{24}$
3	$\lambda^3 A_{33}+\lambda^5 A_{35}$	$\lambda^3 B_{33}+\lambda^5 B_{35}$
4	$\lambda^4 A_{44}$	$\lambda^4 B_{44}$
5	$\lambda^5 A_{55}$	$\lambda^5 B_{55}$

Table 2.2.1: Definition of E_n and D_n

Skjelbreia's solution is calculated by first knowing the periode, waveheight and water depth. Then the wavelength, L, and a coefficient, λ, is calculated by iteration of the following set of equations:

$$F(k,\lambda) = \omega^2 - gk\tanh(kh)\cdot\left(1+\lambda^2 C_1+\lambda^4 C_2\right) = 0, \tag{2.2.14}$$

$$f(\lambda,k) = \frac{kH}{2} - \left(\lambda+\lambda^3 B_{33}+\lambda^5\left(B_{35}+B_{55}\right)\right) = 0. \tag{2.2.15}$$

These are solved iteratively with initial guesses from third order stokes until a converged solution is reached.
The velocity components and accelerations are then to be obtained by differentiation of the velocity potential.

$$u = c_\omega \sum_{j=1}^{5} jD_j \cosh jk(z+h)\cos j\theta \tag{2.2.16}$$

$$w = -c_\omega \sum_{j=1}^{5} j\cdot D_j \sinh jk(z+h)\sin j\theta \tag{2.2.17}$$

$$\frac{\partial u}{\partial x} = c_\omega k \sum_{j=1}^{5} j^2\cdot D_j \cosh jk(z+h)\sin j\theta \tag{2.2.18}$$

$$\frac{\partial u}{\partial z} = c_\omega k \sum_{j=1}^{5} j^2\cdot D_j \sinh jk(z+h)\cos j\theta \tag{2.2.19}$$

2.2.2.2 Taylor Expansion Above Mean Free Surface

To obtain velocities and accelerations above z=0, we utilise a Taylor expansion, as is done in the derivation of Stokes Wave Theory. The Taylor expansion allows us to evaluate the properties for $0 < z < \zeta$. All variables are obtained at $z = 0$.

$$\begin{aligned} f(z) = &(f_1 + f_2 + f_3 + f_4 + f_5) + z\frac{\partial\left(f_1 + f_2 + f_3 + f_4\right)}{\partial z} \\ &+ \frac{z^2}{2}\frac{\partial^2\left(f_1 + f_2 + f_3\right)}{\partial z^2} + \frac{z^3}{6}\frac{\partial^3\left(f_1 + f_2\right)}{\partial z^3} + \frac{z^4}{24}\frac{\partial^4 f_1}{\partial z^4} + \mathcal{O}(z^6), \end{aligned} \tag{2.2.20}$$

where f_1 through f_5 represent the five terms each variable consist of.

2.2.2.3 Limitations with Stokes Fifth Order Waves

For all stoke waves, except first order, it is assumed that $\mathcal{O}(h/L) = 1$. In shallow water where $\frac{h}{L} \ll 1$ a secondary wave crest occur which is not observed in nature. This unproportionately large second order term occurs for $h/L < 0.10 - 0.15$ in Stokes fifth order theory. For lower order theory, this phenomenon is observed for larger h/L values. To summarise the assumptions made during the derivation of stoke waves, the flow is assumed to be potential flow, and symmetrical about the wave crest.

2.2.2.4 Ursell number

Ursell (1953) defined a non-dimensonal number as

$$Ur = \frac{H\lambda^2}{h^3} \tag{2.2.21}$$

Multiple papers have discussed the importance of the Ursell number with regards to Stoke waves and its validity. The consensus seem to be that Stoke waves are valid for values up to $Ur \approx 40$ (Fenton John D., 1985). For higher Ursell numbers, cnoidal wave theory has shown to obtain more accurate results as shown by Hedges (1995).

2.3 Wave Forces on Circular Cylinders

As slender circular cylinders are a highly utilised shape in the marine environment, there exists several theories to analyse the wave forces acting on the cylinder. Many of whom is based on potential theory. The three theories which dominate the field is Malenica and Molin (1995a), the Morison's equation and the FNV theory by Faltinsen et al. (1995). These theories give a fairly good approximation of the forces, but it still does not exist a theory capable of giving accurate results for all structure fluid interaction problems.

2.3.1 KC - Number

To categorise the relationship between the flow velocity and period for a sinusoidally oscillating flow $U = U_{amplitude}\sin(\omega t)$, Keulegan and Carpenter (1958) defined a parameter (hereinafter referred to as the KC number) as:

$$KC = \frac{U_{amplitude} * T}{D}. \tag{2.3.1}$$

Where T and D is the period and diameter, respectively. The KC number has shown to be a fairly good way to describe the flow-field and the forces arising. The KC number is heavily impacting the degree of asymmetry in the wake and the amount of vortexshedding occurring. Bearman, Downie, et al. (1985) state that the onset of asymmetrical features occur at KC=7, three years later Bearman, Obasaju, et al. (1988) presented a paper where the data suggested onset of asymmetry at KC=5.

2.3.2 Inviscid Flow Calculation for 2D Uniform Flow

If potential flow is assumed, the horizontal drag force acting at a cylinder in 2D uniform flow described as

$$F_x = \left(\rho\frac{\pi D^2}{4} + a_{11}^{(2D)}\right)\frac{\partial u}{\partial t} \tag{2.3.2}$$

where a_{11} is the 2D added mass coefficient.

$$a_{11}^{(2D)} = \rho a^2\pi = \rho\frac{\pi D^2}{4} \tag{2.3.3}$$

To generalise one introduce C_M, the coefficient of inertia, such that the equation gets the commonly used form

$$F_x = C_M\rho\frac{\pi D^2}{4}\frac{\partial u}{\partial t} \tag{2.3.4}$$

2.3.3 Morison's Equation

The Morison equation is a widely used prediction method to predict hydrodynamic loads. Because of its simplicity, especially when combined with first order wave theory, it is a quick and simple tool to get a load estimation. The equation is divided into two terms; one represent the mass forces and the other the viscous forces acting on the cylinder. The horizontal force per unit length of the vertical cylinder, dF_x, is given by Morison's equation as:

$$dF_x = \underbrace{\rho\frac{\pi}{4}D^2C_M\partial u/\partial t dz}_{\text{Mass force}} + \underbrace{\frac{1}{2}\rho DC_D|u|udz}_{\text{Drag force}}, \tag{2.3.5}$$

where ρ is the water density, D is the cylinder diameter, a_1 and u are the horizontal acceleration and velocity of the undisturbed fluid at the mid-point of the strip. By assuming long wave approximation, ie. that the waves are long compared to the cylinder radius, such that the cylinder do not deflect the waves, the wave kinematics is taken from the undisturbed potential. Long wave approximation requires that the wave length is five times the diameter of the structure:

$$\frac{\lambda}{D} > 5 \tag{2.3.6}$$

C_M and C_D are the mass and drag coefficients, respectively.

The mass force term in Morison's equation could be recognised as the potential theory force from Equation 2.3.4

$$dF_x = \underbrace{(\frac{\rho\pi D^2}{4} + a_{11})\partial u/\partial t dz}_{\text{Mass force}}. \tag{2.3.7}$$

This is the most common version of the Morison equation. However, a modification has been introduced where the total advection term ($\partial u/\partial t + u\partial u/\partial x + w\partial u/\partial z$) is substituted for $\partial u/\partial t$.

$$\begin{aligned} dF = \rho\pi D^2/4 C_m(\partial u/\partial t + u\partial u/\partial x + w\partial u/\partial z) \\ +\rho C_d D/2|u|u \end{aligned} \tag{2.3.8}$$

The total advection Morison equation is almost similar the FNV theory. The difference will be pointed out after the latter is derived.

2.3.3.1 Calculation of C_M and C_D

The coefficients in the Morison equation can be obtained from experiments by Fourier averaging. Recall the force acting on the cylinder as:

$$-\int p\hat{n}ds = F_x = \rho\frac{1}{2}C_D D U_\infty \mid U_\infty \mid + \rho\frac{\pi}{4}D^2 C_M \dot{U}_\infty. \tag{2.3.9}$$

First multiply Equation 2.3.9 by U_∞ to simplify the equation:

$$\int_{n_1 T}^{n_2 T} F_{CFD} U_\infty dt = \rho\frac{1}{2}C_D D \int_{n_1 T}^{n_2 T} U_\infty \mid U_\infty \mid U_\infty dt + \rho\frac{\pi}{4}D^2 C_M \cancelto{0}{\int_{n_1 T}^{n_2 T} \dot{U}_\infty U_\infty dt}, \tag{2.3.10}$$

by reorganising one obtain the drag coefficient:

$$C_D = \frac{\int_{n_1 T}^{n_2 T} F_{CFD} U_\infty dt}{\rho\frac{1}{2}D \int_{n_1 T}^{n_2 T} U_\infty \mid U_\infty \mid U_\infty dt}. \tag{2.3.11}$$

Similarly the equation could be simplified by multiplying with $\dot{U}_\infty$:

$$\int_{n_1 T}^{n_2 T} F_{CFD} \dot{U}_\infty dt = \rho\frac{1}{2}C_D D \cancelto{0}{\int_{n_1 T}^{n_2 T} U_\infty \mid U_\infty \mid \dot{U}_\infty dt} + \rho\frac{\pi}{4}D^2 C_M \int_{n_1 T}^{n_2 T} \dot{U}_\infty \dot{U}_\infty dt, \tag{2.3.12}$$

By reorganising, the inertia coefficient is obtained:

$$C_M = \frac{\int_{n_1 T}^{n_2 T} F_{CFD} \dot{U}_\infty dt}{\rho\frac{\pi}{4}D^2 \int_{n_1 T}^{n_2 T} \dot{U}_\infty \dot{U}_\infty dt}. \tag{2.3.13}$$

2.3.4 FNV

Faltinsen et al. (1995) developed a diffraction based theory, capable of capturing higher order loads. Like the traditional diffraction theory it is assumed that $\zeta, D \ll L$. However, contradictory to traditional theory we allow $\mathcal{O}(k\zeta) \approx \mathcal{O}(ka) \ll 1$. This extension of validity make sure the theory includes severe sea states. Initially the theory was limited to infinite water depths and regular incident waves. Kristiansen and Faltinsen (2017a). generalised the theory to include arbitrary wave kinematics i.e finite water depths.

2.3.4.1 Derivation of the FNV Theory

A brief introduction to the derivation of the theory will be presented. For full derivation see Kristiansen and Faltinsen (2017a)
First, assume the total wave potential to consist of three main parts, namely incident wave potential, linear diffraction potential and higher order diffraction potential - $\phi_{Total} = \phi_{Incident} + \phi_{Diffraction} + \psi$. ψ approximates the higher order free surface condition (to third order) and satisfies the Laplace equation for 3 dimensions.
The domain is then subdivided to two complementary domains such that

	Inner	Outer
	Order	Order
r	$\mathcal{O}(a)$	$\mathcal{O}(L)$
a	$\mathcal{O}(1)$	
h	$\mathcal{O}(1/\epsilon)$	

Table 2.3.1: Subdomain division, a - radius, L - wavelength, ϵ - perturbation prameter

The parameter ϵ is a small pertubation parameter such that the linear wave slope for the incident waves and the non-dimensional cylinder radius are of order ϵ. ($k\zeta_a = \mathcal{O}(\epsilon) = ka$)

2.3.4.1.1 Inner Region

For the inner domain, let $\epsilon \to 0$, from Table 2.3.1 it is obvious that r remains constant whereas the length $h \to \infty$, the velocity field thus appears to be constant along the cylinder centre:

$$\frac{\partial \phi}{\partial z} \ll \frac{\partial \phi}{\partial x}, \frac{\partial \phi}{\partial y} \tag{2.3.14}$$

given:

$$\partial/\partial z = \mathcal{O}(\epsilon) \tag{2.3.15}$$

Because the horisontal derivatives are dominating, the Laplace equation neatly reduces to two dimensions. By Taylor expanding the linear component of the diffraction potential from (x,y)=(0,0), we obtain:

$$\phi_{\text{Inner}} = \phi_I|_{x=0,y=0} + (x + \phi_{11}) \left.\frac{\partial \phi_I}{\partial x}\right|_{x=0,y=0} + \left(\frac{1}{2}x^2 + \phi_{21}\right) \left.\frac{\partial^2 \phi_I}{\partial x^2}\right|_{x=0,y=0} + f(z,t) + \mathcal{O}\left(\epsilon^4\right) \tag{2.3.16}$$

Where ϕ_{ij} satisfy 2D Laplace equation and the impermeability condition at the cylinder surface.

$$\frac{\partial}{\partial n}\left(x+\phi_{11}\right)\Big|_{r=a}=0 \quad \text{and} \quad \frac{\partial}{\partial n}\left(\frac{1}{2}x^2+\phi_{21}\right)\Big|_{r=a}=0, \tag{2.3.17}$$

n is used to denote the normal vector of the body pointing outwards from the body. We have included an arbitrary function f, as the inner solution misses a boundary condition. The inner domain is too small to utilise the far field condition. This function is found by matching the inner and outer potential as they must be equal at the boundary region.

2.3.4.1.2 Outer Region

The solution for the outer region is obtained by solving the three-dimensional Laplace equation and a far field condition. Note that there is no restriction to satisfy the body boundary condition. When the outer solution is found, it is matched with the inner solution to obtain the unknown, f. Faltinsen (1999) showed that this f do not result in forces below the fifth order and is therefore neglected.

The higher order scatter potential is found by the following formula.

$$\left(\frac{\partial^2\psi}{\partial t^2}+g\frac{\partial\psi}{\partial z}\right)\Big|_{z=\zeta}=-2\nabla\phi\cdot\nabla\frac{\partial\phi}{\partial t}-\frac{1}{2}\nabla\phi\cdot\nabla(\nabla\phi\cdot\nabla\phi)\Big|_{z=\zeta} \tag{2.3.18}$$

Close to the surface, ψ is dominated by the vertical gradient, thus it is assumed:

$$\frac{\partial^2\psi}{\partial t^2}\ll g\frac{\partial\psi}{\partial z}. \tag{2.3.19}$$

The potential for ψ is only calculated for the inner region, we assume that the surface is a plane with constant height ($\zeta_{I1}|_{x=0,y=0}$). The BVP was solved by Faltinsen et al. (1995).

$$F^{\psi}=\rho\pi a^2\frac{4}{g}u^2\frac{\partial u}{\partial t}|_{x=0,y=0} \tag{2.3.20}$$

The force component from the linear diffraction potentials is given as

$$dF'(z,t)=-\int_0^{2\pi}p\cdot N_x a d\theta. \tag{2.3.21}$$

N denotes the surface normal in x direction. We then find the pressure according to Bernoulli equation and carry out the integration to obtain the following:

$$dF'(z,t)=\rho\pi a^2\left(\frac{\partial u}{\partial t}+u\frac{\partial u}{\partial x}+w\frac{\partial u}{\partial z}\right)+a_{11}\left(\frac{\partial u}{\partial t}+w\frac{\partial u}{\partial z}\right) \tag{2.3.22}$$

The total force is then the sum of all the force components

$$F_x(t)=\int_{-h}^{\zeta}dF'(z,t)dz+F^{\psi}. \tag{2.3.23}$$

The difference between the previously mentioned advection Morison for the first harmonic force is related to the term $\partial u/\partial x$. In Morison equation the term reads $C_M\partial u/\partial x$, whereas in the FNV theory $\partial u/\partial x$. This leads to $((C_M-1)\partial u/\partial x)$ difference between the theories.

2.4 Expansion of the FNV Theory

Calculation of forces acting on a slender, circular cylinder by the FNV theory neglects viscous effects. Doing a full 3D viscous CFD analysis is simply too computationally heavy. Rather one would prefer a simpler tool, while still being able to introduce viscous effects. Recall the following equation from the FNV theory:

$$dF'(z,t) = \rho\pi a^2 \left(\frac{\partial u}{\partial t} + u\frac{\partial u}{\partial x} + w\frac{\partial u}{\partial z}\right) + a_{11}\left(\frac{\partial u}{\partial t} + w\frac{\partial u}{\partial z}\right). \tag{2.4.1}$$

Observe the terms can be split into 2 groups; terms acting in a horizontal plane dependent on the time derivative and terms dependent on space derivatives.

$$dF'_{time}(z,t) = \rho\pi a^2 \left(\frac{\partial u}{\partial t}\right) + a_{11}\left(\frac{\partial u}{\partial t}\right) \tag{2.4.2}$$

$$dF'_{space}(z,t) = \rho\pi a^2 \left(u\frac{\partial u}{\partial x} + w\frac{\partial u}{\partial z}\right) + a_{11}\left(w\frac{\partial u}{\partial z}\right) \tag{2.4.3}$$

The $dF'_{time}(z,t)$ force could be recognised as the analytic expression for inline force in potential theory (Equation 2.3.4) for a 2D uniform flow. The flow condition with a uniform oscillatory flow can be recreated in a 2D CFD analysis, where viscous forces can be accounted for. The potential flow force is replaced by a 2D CFD force. The new local force at a cross section becomes:

$$dF'(z,t) = dF'_{space}(z,t) + dF_{CFD}(z,t) \tag{2.4.4}$$

where the total force again is found by Equation 2.3.23.

2.5 Expansion of 2D CFD with Navier Stokes Equations

The result from a 2D CFD analysis is obtained by solving the Navier Stokes equation with zero vertical components. Recall the Momentum equation which is solved in a 2D plane. For the sake of simplicity further down the line, utilise cylindrical coordinates.

$$\begin{aligned} r : \rho\left(\frac{\partial v_r}{\partial t} + v_r\frac{\partial v_r}{\partial r} + \frac{v_\theta}{r}\frac{\partial v_r}{\partial \theta} - \frac{v_\theta^2}{r} + v_z\frac{\partial v_r}{\partial z}\right) = -\frac{\partial P}{\partial r} + \\ \mu\left(\frac{\partial}{\partial r}\left(\frac{1}{r}\frac{\partial}{\partial r}(rv_r)\right) + \frac{1}{r^2}\frac{\partial^2 v_r}{\partial \theta^2} - \frac{2}{r^2}\frac{\partial v_\theta}{\partial \theta} + \frac{\partial^2 v_r}{\partial z^2}\right) + \rho g_r. \end{aligned} \tag{2.5.1}$$

With zero vertical components, one obtain the following equation,

$$\begin{aligned} r : \rho\left(\frac{\partial v_r}{\partial t} + v_r\frac{\partial v_r}{\partial r} + \frac{v_\theta}{r}\frac{\partial v_r}{\partial \theta} - \frac{v_\theta^2}{r}\right) = -\frac{\partial P_{2D}}{\partial r} + \\ \mu\left(\frac{\partial}{\partial r}\left(\frac{1}{r}\frac{\partial}{\partial r}(rv_r)\right) + \frac{1}{r^2}\frac{\partial^2 v_r}{\partial \theta^2} - \frac{2}{r^2}\frac{\partial v_\theta}{\partial \theta}\right) + \rho g_r, \end{aligned} \tag{2.5.2}$$

which is solved by a CFD analysis. As pressure is a linear scalar, assume the pressure could be written as:

$$P = P_{2D} + P_w \tag{2.5.3}$$

namely a 2D pressure, and a 3D contribution. Subtract Equation 2.5.2 from Equation 2.5.1, to gather the terms neglected by assuming 2D flow, to obtain the following relationship:

$$\rho v_z \frac{\partial v_r}{\partial z} - \mu \frac{\partial^2 v_r}{\partial z^2} = -\frac{\partial p_w}{\partial r} \tag{2.5.4}$$

For a monopile in incident wave, an approximation of the vertical velocity can be achieved by assuming a small structure compared to wavelength. The velocity potential is thus assumed to be undisturbed and one utilise the vertical velocity component from the undisturbed potential. As previously discussed, potential theory is generally a good assumption when the flow is not influenced by a body. By assuming viscous effects is negligible, the 3D viscous term is neglected from Equation 2.5.4 ($\mu \frac{\partial^2 v_r}{\partial z^2} \ll \rho v_z \frac{\partial v_r}{\partial z}$). Equation 2.5.4 then simplifies to:

$$\rho v_z \frac{\partial v_r}{\partial z} = -\frac{\partial p_w}{\partial r} \tag{2.5.5}$$

By investigating two 2D CFD analyses from different vertical position, then the term $\frac{\partial u}{\partial z}$ can be approximated with a numerical scheme.

To obtain the pressure acting at a body, Equation 2.5.5 is integrated from far field where we assume the pressure to be known to the body of the cylinder:

$$P_w = P_{Farfield} + \rho \int_{FarField}^{Radius} \frac{\partial p_w}{\partial r} dr. \tag{2.5.6}$$

The force contribution from the pressure acting at the body is included in the pressure from the 2D simulation for a semi 3D result.

$$dF'_w(z,t) = -\int_0^{2\pi} P_w N_x a d\theta. \tag{2.5.7}$$

N denotes the surface normal in x direction.
The CFD-FNV load on a strip then becomes:

$$dF'(z,t) = dF'_{space}(z,t) + dF_{CFD}(z,t) + dF'_w(z,t) \tag{2.5.8}$$

and the total load calculated by integration

$$F_x(t) = \int_{-h}^{\zeta} dF'(z,t) dz + F^{\psi}. \tag{2.5.9}$$

In the case where the coordinate system have a velocity and acceleration, the equations are solved differently as the original total derivative from Equation 2.1.8 gains extra terms. For the special case where the coordinate systems' movement accurately matches the particle velocity v_z the relative velocity between the particles and coordinate system in the vertical direction is zero. The extra terms which originated from the coordinate system movement will zero out and we are left with the same equation.

The additional term described here is a new approach and have, to the authors knowledge, never been utilised before. The accuracy is dependent on a few assumptions, namely:

- The validity of using an undisturbed velocity potential

- The assumption that each strip is independent as there is no information transfer between each CFD analysis

2.5.1 Capturing the Effect of Water Rise-up

Chaplin et al. (1997) described a water rise-up at the rear of the cylinder as a large wave crest is passing the cylinder. The same phenomenon was discussed and visualised by Kristiansen and Faltinsen (2017a). The water rise-up at the rear of the cylinder indicates that the slender body assumption is not perfectly valid. In an effort to explain and include the rise-up effect, a possible explanation was derived. According to Griffin (2020) the vortex strength behind a bluff body, such as a monopile, is dependent on Reynolds number. The velocities closer to the free surface is higher, we thus assume that the vortices shed are stronger. Recall Prandtl lifting-line theory where vortices are used to develop lift at a foil. In 3D these vortices are bounded and runs from infinitely far back of the foil across the span and then back. The same analogy could be used here. Assume the shed vortex could be modelled as a set of bound vortices. As the vortex is strongest at the surface, we assume that some of the vortex sheet bend of further down and thus reduces the vortex strength as illustrated in Figure 2.5.1. The vortices induce a vertical velocity component. If the vorticity can be found from the 2D CFD and the change across each strip can be found, then the induced vertical velocity components could be added to the wave kinematics. Unfortunately, due to limited time this theory was never finished, and could thus not be included. However, it remains a topic of interest as the induced velocities induce a rise-up as visually observed.

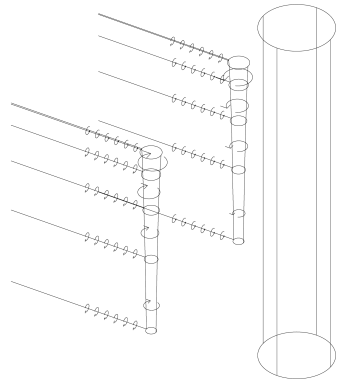

Figure 2.5.1: Vortex sheet behind the monopile

2.6 Computational Fluid Dynamics

2.6.1 Averaged Navier Stokes for Turbulent flows

The Navier Stokes equation govern unsteady turbulent flows, but as these are hard, borderline impossible to solve, a simplification is needed. By time averaging one smoothens out the irregular quantities. We assume that a variable could be split into a time average and fluctuations around the mean value. For example:

$$u = \bar{u} + u' \tag{2.6.1}$$

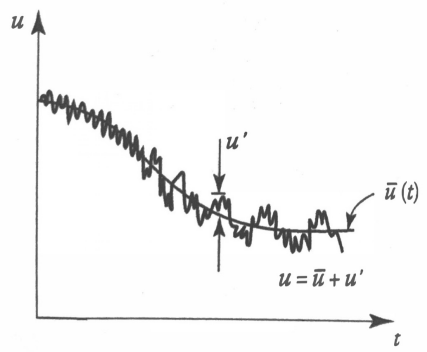

(a) Averaging for RANS

for a variable f:

$$f = \bar{f} + f' \tag{2.6.2}$$

then by definition

$$\bar{f'} = \frac{1}{\Delta t}\int_0^{t_0+\Delta t} f' dt \equiv 0 \tag{2.6.3}$$

note that as $\bar{f'} \equiv 0$ does not imply that the product is zero, the product $f'\bar{f'} \neq 0$. The normalised RMS value of velocity is whats commonly referred to as turbulence intensity. Equation 2.1.8 could be written as

$$\frac{\partial u_i}{\partial t} + \frac{\partial}{\partial x_j}(u_i u_j) = -\frac{\partial p}{\partial x_i} + \nu \frac{\partial^2 u_i}{\partial x_j \partial x_j} \tag{2.6.4}$$

by simply writing out the operators and dividing by ρ.
Insert the fluctuating parameteres on the form as Equation 2.6.2, and obtain the RANS equation.

$$\frac{\partial \bar{u}_i}{\partial t} + \bar{u}_j \frac{\partial \bar{u}_i}{\partial x_j} = -\frac{\partial \bar{p}}{\partial x_i} + \nu \frac{\partial^2 \bar{u}_i}{\partial x_j \partial x_j} - \frac{\partial \tau_{ij}}{\partial x_j} \tag{2.6.5}$$

where

$$\tau_{ij} = \overline{u_i' u_j'} \tag{2.6.6}$$

is referred to as the Reynolds stress term. This term includes six additional unknowns in 3D, and leaves the problem to be closed. The closure problem can be solved using a technique known as turbulence modelling. Continuity equation for a incompressible fluid:

$$\frac{\partial \bar{u}_i}{\partial x_i} = 0 \tag{2.6.7}$$

2.6.2 Boussinesq Eddy Viscosity

As the equation set involves more unknowns than equations, one needs to close the problem. This is an unsolved problem, an approximation is forced by correlating the unknown to variables with known quantities. One of the most common methods are the Boussinesq

Eddy Viscosity proposed by Joseph Boussinesq. The Boussinesq Eddy Viscosity concept build upon the following assumption. As the turbulence intensity in a flow increases, the chaos within the flow increases, and the amount of vortices increase. The more chaos, the more energy the flow can transport. The same could be achieved by simply increasing the viscosity. This is done by adding a turbulent viscosity to the momentum equation such that the smaller vortices do not need to be resolved, and thus save computational effort. The Boussinesq assumption reads:

$$-\overline{\rho u_i' u_j'} = 2\mu_{\mathrm{T}} S_{ij} - \frac{2}{3}\delta_{ij}\left(\mu_{\mathrm{T}}\frac{\partial u_k}{\partial x_k} + \rho\bar{k}\right) \tag{2.6.8}$$

where

$$S_{ij} = \frac{1}{2}\left(\frac{\partial u_i}{\partial x_j} + \frac{\partial u_j}{\partial x_i}\right) \tag{2.6.9}$$

and

$$\bar{k} = \overline{u_i' u_i'}/2 \tag{2.6.10}$$

To solve this equation there still is a few unknowns. These are solved by the turbulence model. There are several options depending on the amount of equations used to close the problem. Most one-equation and zero-equation models rely on experimentally obtained results, whereas two-equation models is closed without the use of experimental results.

2.6.2.1 Turbulence Model

There have been proposed multiple turbulence models to use in CFD, all of whom have their strengths and weaknesses. Amongst these are the $k-\omega$ model, as well as $k-\epsilon$. The $k-\epsilon$ is a successful turbulence model which yeilds accurate results for the flow which it has been tuned for, but suffers from inaccuracy at the near wall treatment as ϵ do not converge to zero. It normally overestimates shear stress and thus delays separation. On the other hand, the $k-\omega$ model has the possibility to enforce a Dirichlet condition at the wall, to more accurately solve the boundary condition. The drawback is the highly dependence on the on the turbulence properties defined at the inlet. The SST $k-\omega$ gives a "best of both worlds" approach, combining the strength of the $k-\epsilon$ and $k-\omega$ model. SST $k-\omega$ model uses $k-\omega$ approach for near-wall treatment and switches to the $k-\epsilon$ formulation free-stream. More information about turbulence model and its properties can be found in the book by Pope (2000) where k, ω, ϵ is defined.

2.6.3 Numerical Stability

The courant number was described by Courant et al. (1967) in regards to numerical stability of explicit schemes. Where stability requires the courant number to be below an upper limit.

$$Co = \frac{\mathrm{abs}(u)\Delta t}{\Delta x} + \frac{\mathrm{abs}(v)\Delta t}{\Delta y} < Co_{\max} \tag{2.6.11}$$

As Holzmann (2019) described, OpenFOAM slightly altered the formula to include the cell volume rather than its side length, but the concept remains the same. A high Courant number means that the fluid travels far through the cell at each time-step. The Courant

number has a direct implication on the time to run an analysis as a low courant number results in more time steps per unit of time. A high courant number is beneficial for computational performance, but might cause instabilities.

2.7 The Numerical Algorithms: SIMPLE, PISO and PIMPLE

As very few analytic solutions of the Navier-Stoke equation exist, numerical methods are used to approximate a solution. To solve the problem one apply numerical techniques. The most common algorithms are named SIMPLE, PISO and PIMPLE.

The momentum equation has four unknowns, of which three are velocity components in addition to the pressure. However, there are only three equations. One thus introduce the continuity equation. Special techniques are applied to solve the system. After some mathematical operations one could obtain a meaningful equation set. The derivation can be found in the book by H. K. Versteeg (2007). The pressure-momentum coupling problem is then solved numerically. The Pimple algorithm is one of the most commonly used for transient problems. Pimple combines the Simple and Piso techniques, on which more information can be found in the book by Moukalled et al. (2016). Within each time-step, a steady state solution is found using an under-relaxation strategy. Then proceed to the next time-step after using outer corrector loops to ensure explicit parts of the equations have reached convergence. As convergence is reached the outer correction loop is left, and the same procedure is done for the subsequent time-step.

2.7.1 Resolving the boundary layer

A wall bounded flow needs to obey the no slip and no penetration boundary condition at the wall. This results in a boundary layer close to the wall. At the wall, viscous forces dominate as the Reynolds stresses are zero. The important dimensionless parameter y^+ measures the viscous lengths from the wall

$$y^+ = \frac{y}{\delta_v} = \frac{u_\tau y}{\nu} \tag{2.7.1}$$

where:

$$u_\tau = \sqrt{\frac{\tau_w}{\rho}} \tag{2.7.2}$$

and:

$$\tau_w = \rho\nu \left(\frac{\partial u_k}{\partial x_k}\right)_{\text{at the body}} \tag{2.7.3}$$

Close to the wall where the viscous force is important, the velocity profile is dependent on the Reynolds number as well as whether the flow is turbulent or not. For oscillatory flow is the point of transition to turbulent flow not well documented, some papers indicate the onset of turbulent structures as early as $Re = 7000$. Fully resolving the boundary layer is crucial to accurately model separation, and the flow in general, close to a body.

Low values of y^+ describes a flow where viscous forces dominate, whereas for $y^+ > 50$ viscous forces are negligible. For $5 < y^+ < 50$ there is a buffer layer between the viscous sublayer and the fully turbulent region. The buffer layer should be avoided. Salim and Cheah (2009) describes the importance of y^+ in mesh generation. They conclude that keeping $y^+ \approx 1$ is desirable for near wall modelling which leads to more accurate computational predictions. An alternative is to keep y^+ in the fully turbulent region and use wall functions to describe the flow as a low y^+ value results in a computationally heavier analysis as the number of cells increase.

2.8 Software

The preferred software for this project was chosen to be the open source CFD code OpenFOAM. Most commercial CFD codes are expensive, whereas OpenFOAM is free of charge. Sarode et al. (2017) benchmarked OpenFOAM against costly commercial software and concluded that the results obtained by OpenFOAM shows the same behaviour. The downside is the lack of graphical user interface and generally poor user friendliness. As soon as the user has overcome the apparent issues getting started, OpenFOAM is a really powerful tool and being run on linux has great capabilities being connected with Python to automise the process of setting up cases for analysis.

Chapter 3

Experiments

A paper by Kristiansen and Faltinsen (2017a) based on experiments originally carried out by former Statiol (now Equinor). The first tests were conducted on 2017 at Tyholt. The same model and set-up still exist at NTNU. Experiments were carried out using the same set up and model.

3.1 Test Setup

The wind turbine monopile was mounted in Lilletanken at Tyholt, Trondheim. The scale of the model is 1:48. The diameter of the model is 0.144 meters and a water-depth of $h = 0.5625$ meters. 4 wave-probes were mounted upstream of the monopile, two at same height and two downstream. See Figure 3.1.1 for a photo of the lab set-up.

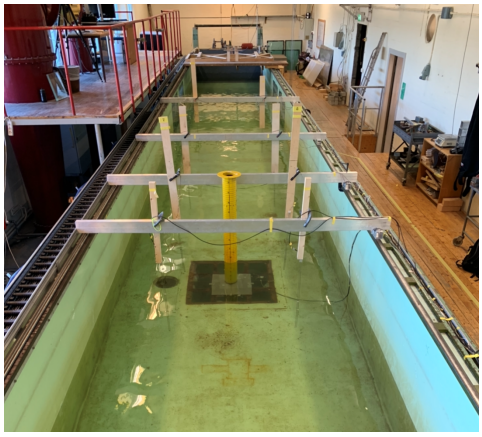

Figure 3.1.1: Photo of model test lab set-up. The wave maker is seen in the end of the tank.

As seen in the figure, the wave probes were placed in the center between the tank walls and the monopile, on each side. The distances, in wave propagation direction between the

wave probes and the dimensions of the tank are given in Figure 3.1.2.

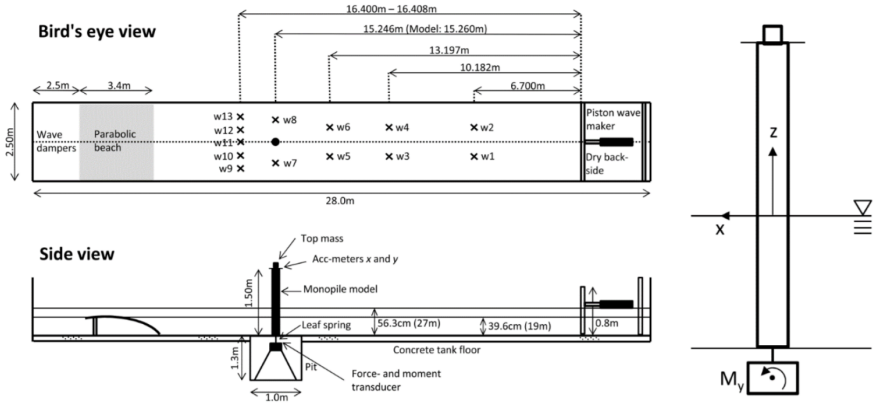

Figure 3.1.2: Lab set-up

During the experiments, the free surface elevation was measured at 8 different positions. Horizontal force and overturning moment in the bottom of the monopile were measured by a force transducer, using strain measurements. All sensors had been calibrated beforehand. The focus in the experiments was neither the loads nor moment, but visual data of the interaction problem and vortex generation.

3.2 Results

A discrepancy in the incoming waves was observed, causing unexpected loads. Kristiansen and Faltinsen (2017a) observed the same phenomenon concluded it was caused by free parasitic waves excited from the wavemaker. Adding a correction signal at a frequency of 2ω solved the matter for Faltinsen. The same analogy was applied in these experiments, but as time was limited between other ongoing experiments, proper tuning of the correction signal was never achieved. The parasitic wave was reduced to a point where it was no longer visually observable, however it still had a slight impact on the loads. However, it still had a slight impact on the loads. As the experiment had been carried out multiple times with proper tuning, a lot of data was readily available. The data presented below is data obtained by previous experiments in the same tank and the same rig. Parts of the data has been previously published.

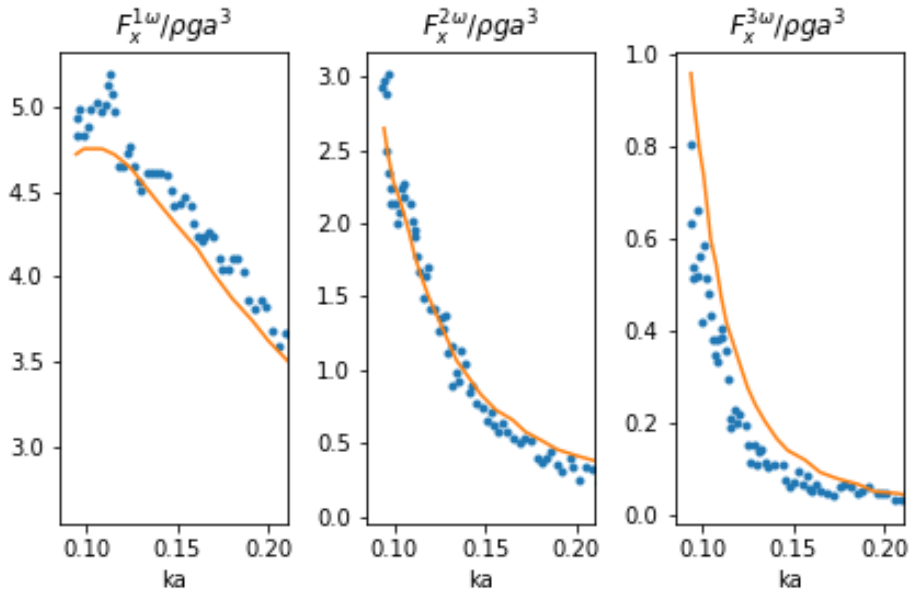

Figure 3.2.1: First three force harmonics from Experiments (•), FNV theory (–) for $H_1/\lambda = 1/25$

The data shows inconsistencies between the FNV theory and the experimental data with regards to third order forces. Similar plots for $H_1/\lambda = 1/30$ and $H_1/\lambda = 1/40$ are shown in section A.2. The data for $H_1/\lambda = 1/30$ shows a similar inconsistency, whereas for $H_1/\lambda = 1/40$ there are generally good agreement between experiments and theory. The same experimental data will be further investigated and compared to the newly developed CFD-FNV theory in chapter 6.

3.2.1 Visual Observation

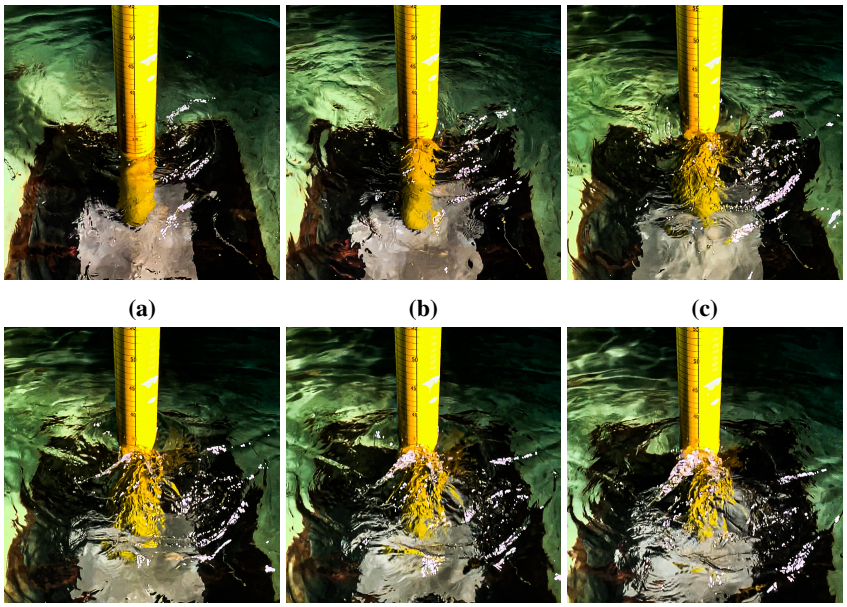

Figure 3.2.2: Snapshots of the flow behind the cylinder with T=2.165 s and steepness of $H_1/\lambda = 1/25$

From Figure 3.2.2 where a wave-crest is passing the mono-pile. The first picture is taken 90 degrees before the wave crest, and the last one right after the crest has passed. Observe the water rise-up occurring as the wave crest hits the monopile. The rise-up is narrow at first, and seems to be consisting of water originating from below the water surface. As the wave passes, the rise-up reaches its maximum height and dissipates.

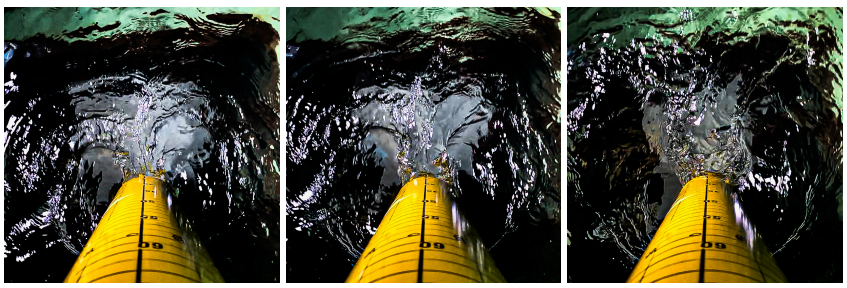

Figure 3.2.3: Snapshots of the flow behind the cylinder seen from above with T=2.165 s and steepness of $H_1/\lambda = 1/25$

In Figure 3.2.3 the the first picture is taken as one see the first sign of rise-up. Again

observe the narrow peak. The next picture is where the peak is closing up on its maximum height. A crucial takeaway in this picture is the formation of two nearly symmetrical vortices occurring in the water surface. This is an indication that the water rise-up could origin from the vortex sheet as discussed in subsection 2.5.1.

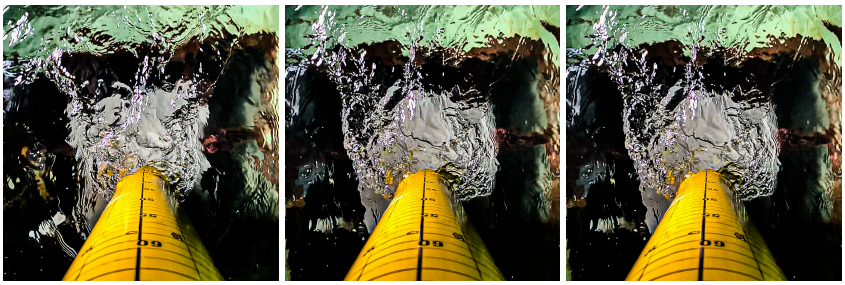

(a) **(b)** **(c)**

Figure 3.2.4: Snapshots of the flow behind the cylinder seen from above with T=2.165 s and steepness of $H_1/\lambda = 1/25$

After the peak breaks, a highly turbulent environment arises behind the cylinder. This highlights the importance of proper turbulence modeling and a sufficiently fine grid when doing CFD analysis on this phenomenon. By neglecting 3D effects, the disturbances of the fluid will probably be less turbulent and the validity of both slender body assumption and the cross flow principle should be discussed.

Chapter 4

Numerical Model

4.1 Mesh Structure

A structured grid comes with several advantages and drawbacks compared to unstructured grids. Unstructured grids are easy to create using a meshing tool and allows for complex geometries, whereas the process of creating a a structured grids can tedious. A structured grid using only hexahedral cells results in a higher orthogonality and a more efficient use of memory, allowing for faster computation. A pure hexahedral mesh is therefore utilised in this report and created using OpenFOAMs *blockMesh* tool.

4.1.1 Block Mesh

A set of blocks subdivides the domain, illustrated in Figure 4.1.1, into smaller parts to ensure sufficient control. The boundary layer is kept within a block to ensure required mesh quality. The boundary layer is estimated by laminar theory:

$$\delta^{99} = 4.6 \cdot \sqrt{\frac{2\nu}{\omega}} \tag{4.1.1}$$

One can then ensure that enough cells to capture the boundary layer effect are put within the boundary layer. A second control circle are placed around the cylinder to capture the vortices shedding from the cylinder, the size of this block is chosen to be $10r$ as this should be sufficient to keep the vortices within this region of high quality mesh. The domain is outwards transformed to a square. The cell size is the same across block boarders to avoid large changes of cell size.

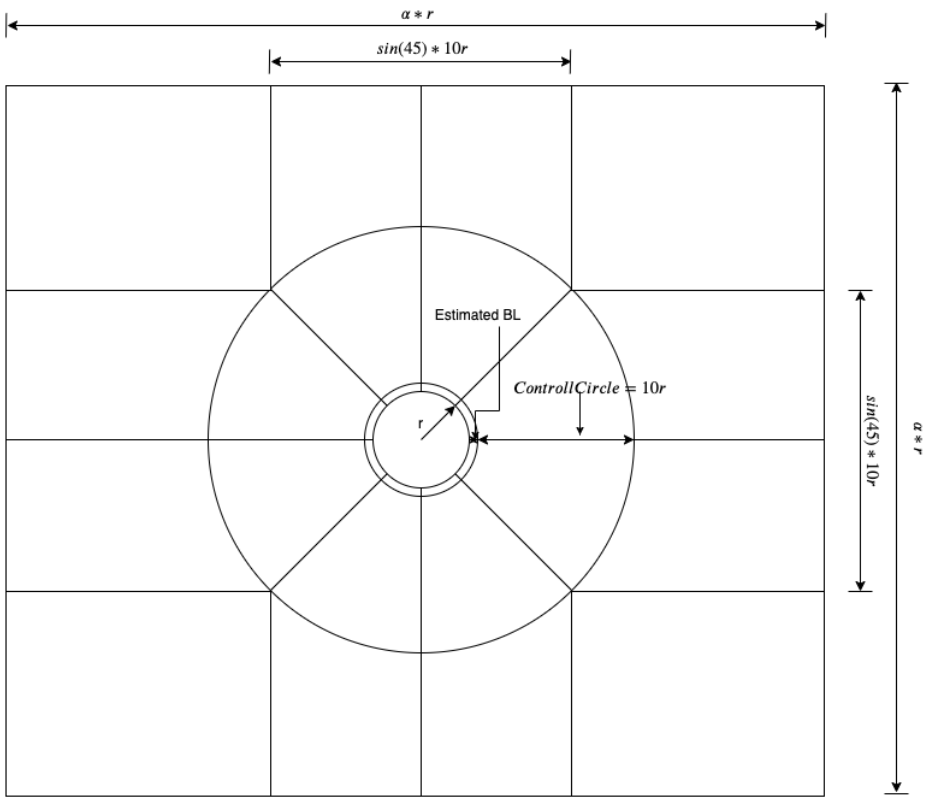

Figure 4.1.1: Block discretisation of the computational domain

4.2 Boundary Conditions

The cylinder is enclosed in a 2D domain. We assume that the domain is sufficiently large, and apply boundary conditions at the boundary. The boundary conditions should mimic the physics involved as best as possible. The oscillatory flow is pressure-driven as this showed to highly improve stability from a velocity forced flow. The pressure enforced on the boundary according to the following equations. Recall the Navier Stokes Equation 2.1.8, and assume only pressure-force is acting.

$$\frac{Du}{Dt} = -\frac{1}{\rho}\nabla p \tag{4.2.1}$$

in x direction:

$$\frac{\partial u}{\partial t} + u\frac{\partial u}{\partial x} + v\frac{\partial v}{\partial y} = -\frac{1}{\rho}\frac{\partial p}{\partial x} \tag{4.2.2}$$

Assume that the flow velocity do not change trough the domain to satisfy continuity:

$$\frac{\partial u}{\partial t} = -\frac{1}{\rho}\frac{\partial p}{\partial x} \tag{4.2.3}$$

To obtain additional equation to close the equation set, the pressure at the inlet is defined as the negative pressure at the outlet.

$$p(\frac{L}{2}) \equiv -p(-\frac{L}{2}) \tag{4.2.4}$$

The pressure can be obtained by solving for $p(\frac{L}{2})$:

$$\int_{-\frac{L}{2}}^{\frac{L}{2}} \frac{\partial p}{\partial x} dx = -\rho \int_{-\frac{L}{2}}^{\frac{L}{2}} \frac{\partial u}{\partial t} dx, \tag{4.2.5}$$

$$p(\frac{L}{2}) = -\frac{1}{2}\rho L \frac{\partial u}{\partial t}. \tag{4.2.6}$$

At the right and left boundary, hereinafter referred to as inlet/outlet, the pressure is thus defined according to Equation 4.2.6. We assume that the inflow is perpendicular to the inlet and outlet, and that the flow at the top and bottom only have a component in the flow direction through the domain. The boundary conditions applied is listed in Table 4.2.1:

Boundary Contidtions			
Variabel	**Cylinder**	**Top and Bottom**	**Inlet Outlet**
pressure	zeroGradient	zeroGradient	uniformTotalPressure
velocity	noSlip	slip	pressureNormalInletOutletVelocity
k	$fixedValue^{[0]}$	$fixedValue^{[1]}$	$fixedValue^{[1]}$
omega	$fixedValue^{[2]}$	$fixedValue^{[3]}$	$fixedValue^{[3]}$
nut	nutkWallFunction	calculated	calculated

Table 4.2.1: Boundary conditions

where the values inserted are individual for each analysis and calculated based on the following:

$$[0]: \quad k = 0 \tag{4.2.7}$$

$$[1]: \quad \frac{10^{-5}U_\infty^2}{Re_L} < k_\infty < \frac{0.1U_\infty^2}{Re_L} \tag{4.2.8}$$

$$[2]: \quad \omega_{wall} = 10\frac{6\nu_\infty}{\beta_1 \left(\Delta y_{wall}\right)^2} \tag{4.2.9}$$

where $\beta_1 = 0.075$

$$[3]: \quad \frac{U_\infty}{L} < \omega_\infty < \frac{10U_\infty}{L} \tag{4.2.10}$$

in the equations above, U_∞ is calculated as the RMS value over one periode of the inlet velocity. The equations are taken from Menter (1994) as well as Langley Research Center (n.d.). The velocity is initialised to match the phase at the beginning of each analysis.

4.3 OpenFOAM model

The OpenFOAM model was created by trial and error, as well as input from relevant literature. A brief introduction was given in section 2.6. More thorough derivations and explanations are readily available from *Mathematics, Numerics, Derivations and OpenFOAM®* by Holzmann (2019) and *The Finite Volume Method in Computational Fluid Dynamics* by Moukalled et al. (2016).

4.3.1 Solvers

The PIMPLE was the chosen solver algorithm. As previously mentioned this is a merged PISO and SIMPLE algorithm.
The following setup was used for the PIMPLE algorithm:

Pimple Settings	
Variable	**Value**
nNonOrthogonalCorrectors	1
nCorrectors	3
nOuterCorrectors	500
Residual control	
U	$1e-5$
p	$1e-5$
k	$1e-4$
omega	$1e-4$
Relaxation Factors	
U	0.7
p	0.3
k	0.7
omega	0.7

Table 4.3.1: Pimple Settings

Solvers				
Variable	**Solver**	**Tolerance**	**Smoother**	**Preconditioner**
p	GAMG	$1e-5$	DICGaussSeidel	-
U	PBiCG	$1e-8$	-	DILU
k	smoothSolver	$1e-5$	symGaussSeidel	-
omega	smoothSolver	$1e-5$	symGaussSeidel	-

Table 4.3.2: Solvers

As the system of equations to be solved is big, solving it efficiently and accurately is important. Solving the equations is done by combining a multi-grid method (GAMG) using numerical methods with the preconditioned bi-conjugate gradient (PBiCG). Diagonal based incomplete LU (DILU) preconditioner were used for the velocity . The solvers are chosen such to achieve the best possible accuracy combined with stability. They are all based on *Discretization Schemes – How to Choose the Schemes* by OpenFoam adviser Guerrero (n.d.).

4.3.2 Schemes

. Additional information can be found in (Moukalled et al., 2016).

Numerical Schemes		
Variable	**Scheme**	**Precision**
	Time Schemes	
ddt	CrankNicolson 0.75	$\approx \mathcal{O}\left(\delta t^2\right)$
	GradSchemes	
default	cellMDLimited Gauss linear 0.5;	$\mathcal{O}\left(\Delta x^2, \Delta y^2\right)$
U	cellMDLimited Gauss linear 0.5;	$\mathcal{O}\left(\Delta x^2, \Delta y^2\right)$
	DivSchemes	
phi, U	Gauss linearUpwind	$\mathcal{O}\left(\Delta x^2, \Delta y^2\right)$
phi, k	Gauss linearUpwind	$\mathcal{O}\left(\Delta x^2, \Delta y^2\right)$
phi, omega	Gauss linearUpwind	$\mathcal{O}\left(\Delta x^2, \Delta y^2\right)$
phi, nuEff*dev2(T(grad(U)))	Gauss linear	$\mathcal{O}\left(\Delta x^2, \Delta y^2\right)$
	laplacianSchemes	
diffusive terms	Gauss linear limited 1	$\mathcal{O}\left(\Delta x^2, \Delta y^2\right)$

Table 4.3.3: Schemes

The schemes are chosen based on a compromise between stability and accuracy. Mesh quality impacts the choise, where a low quality mesh needs a more stable scheme. The above chosen schemes are chosen based on testing and the input from *Discretization Schemes – How to Choose the Schemes* by OpenFoam adviser Guerrero (n.d.).

Chapter 5

Mesh Convergence

Each block shown in Figure 4.1.1 is meshed into a finer grid. As the grid definition depends on multiple variables, finding out their dependence is an extremely time consuming task. To simplify this problem, free variables were locked in dependence to others. The first cell height at the cylinder surface is calculated through estimation of $y+1$ with the equations presented in subsection 2.7.1 to ensure $y+ \approx 1$. The amount of cells around the cylinder was chosen to be 400, such that each cell covered less than 1 degree, as advised by prof. Bjørnar Pettersen. This should be sufficient to accurately capture the point of flow separation. The cell size radially was defined with a growth-rate from the first cell hight. Separate growth-rate was defined inside the estimated boundary layer and for the domain control circle. Five cases of the inner growth-rate was tested. $InnerGrowthRate = \{1.2, 1.15, 1.1, 1.08, 1.05\}$. The outer growth-rate was defined as a multiple of this in such a manner:

$$OuterGrowthRate = (InnerGrowthRate - 1) * Factor + 1, \tag{5.0.1}$$

where three different factors where tested. $Factor = \{0.25, 0.125, 0.1\}$.

The mesh convergence was conducted by first initialising the fluid with three oscillations on a general mesh, The result then were mapped onto the new mesh to be tested. One oscillation to adjust to the new mesh, and then five oscillations where the force coefficients where calculated. This saved computational time as the initialisation oscillations did not have to be performed at each case.

A subset of the meshes are shown in Figure 5.0.1 through Figure 5.0.4 to give a visual indication on the grid generation.

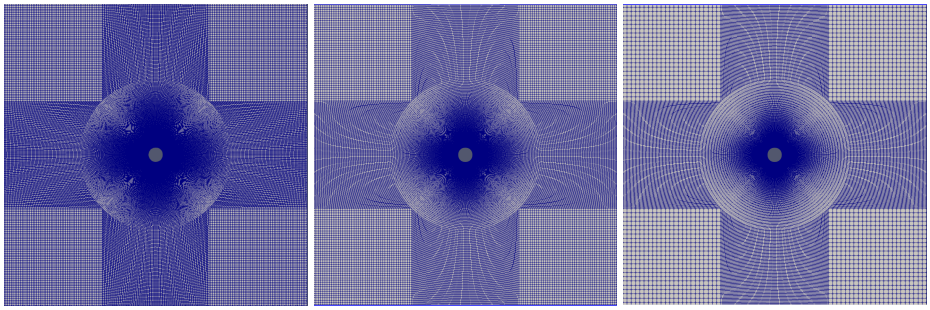

(a) **(b)** **(c)**

Figure 5.0.1: Domain with Factor 0.1, 0.125 and 0.25, reading from left to right, with the grading factor in the boundary layer at 1.2

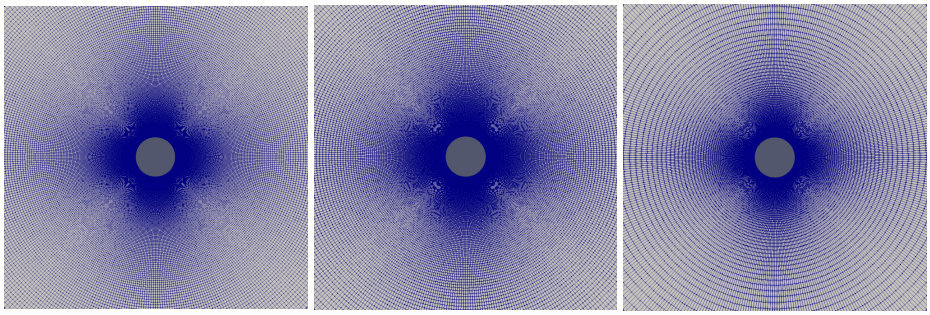

(a) **(b)** **(c)**

Figure 5.0.2: Distance 10r to each side, with Factor 0.1, 0.125 and 0.25, reading from left to right, with the grading factor in the boundary layer at 1.2.

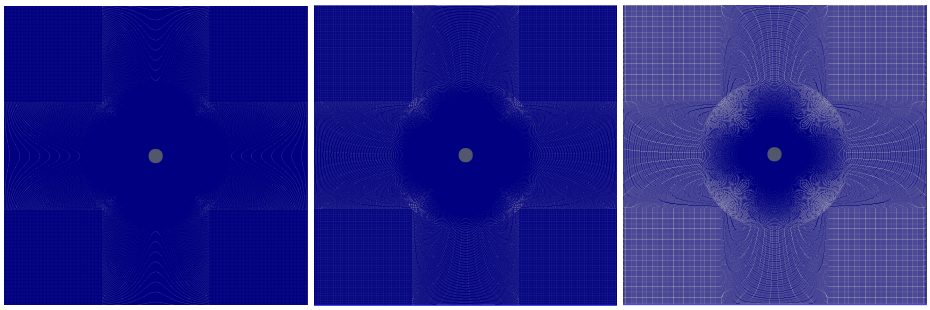

(a) **(b)** **(c)**

Figure 5.0.3: Domain with Factor 0.1, 0.125 and 0.25, reading from left to right, with the grading factor in the boundary layer at 1.05.

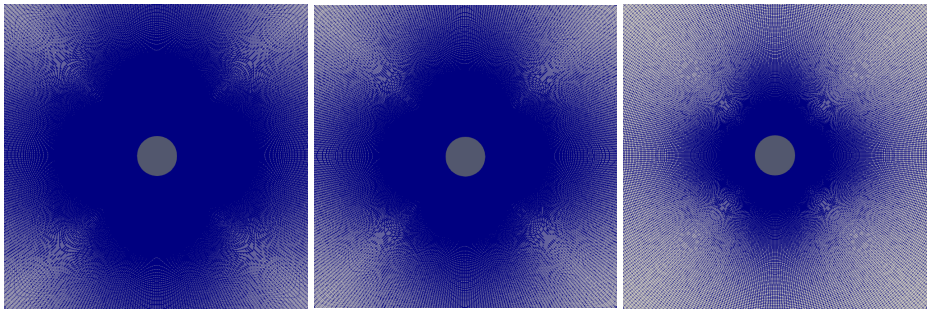

(a) (b) (c)

Figure 5.0.4: Distance 10r to each side, with Factor 0.1, 0.125 and 0.25, reading from left to right, with the grading factor in the boundary layer at 1.2.

5.1 Mesh Convergence Results

Each mesh had a series of tests conducted for a range of KC and Reynolds numbers. Not all of them yielded viable results. Due to computational time limits not all were tested. The accuracy of the solution is dependent on the number of grid cells as much as their positioning. The first thing observed is that the lower KC numbers are more or less independent of mesh quality within the region investigated, whereas the higher KC numbers showed a great dependance.

C_M and C_D are extracted as shown in subsubsection 2.3.3.1. A total of eight periodes, where the 3 first are considered as initialisation, before the next five is used for calculating C_M and C_D. The extreme values were discarded, and the average over the remaining three is used as the final value. The standard deviation is plotted as a vertical line in all plots below.

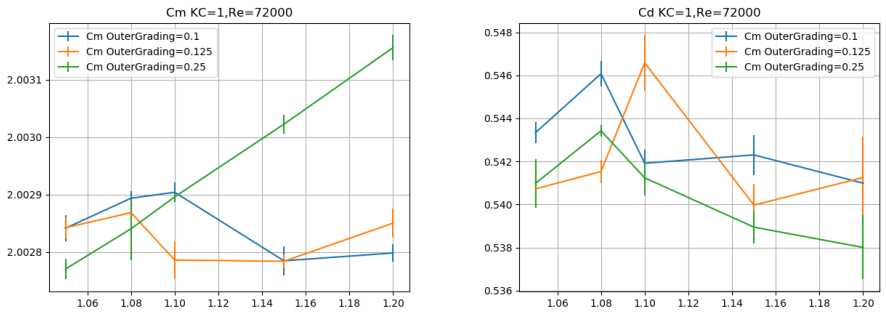

(a) (b)

Figure 5.1.1: Mesh convergence for KC=1.

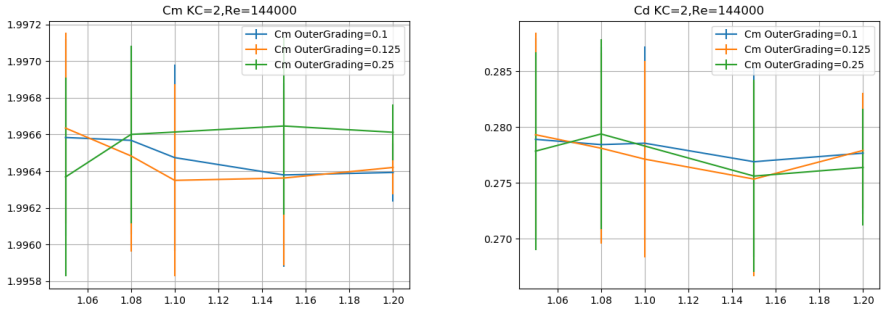

(a) **(b)**

Figure 5.1.2: Mesh convergence for KC=2.

The lower KC numbers shows early convergence and small mesh dependence for C_M. For KC=1 and a low Reynolds number, capturing the boundary layer effect is important to estimate drag. This thus indicate a finer grid is necessary. A coarse CFD mesh generally under-predicts the drag force for low KC numbers as the viscous sublayer is not fully resolved. Experimental data shows a high value for C_D at KC=1

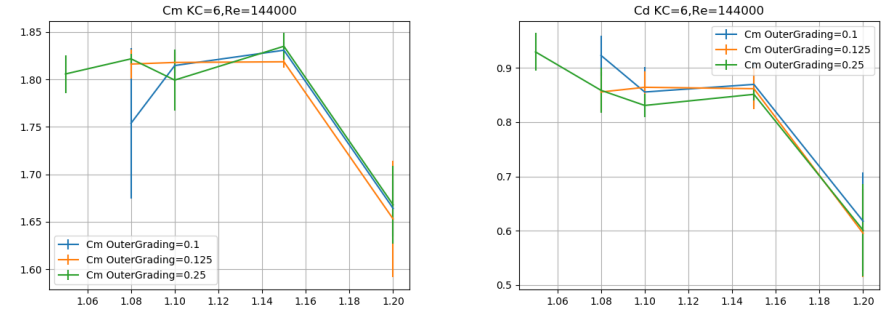

(a) **(b)**

Figure 5.1.3: Mesh convergence for KC=6.

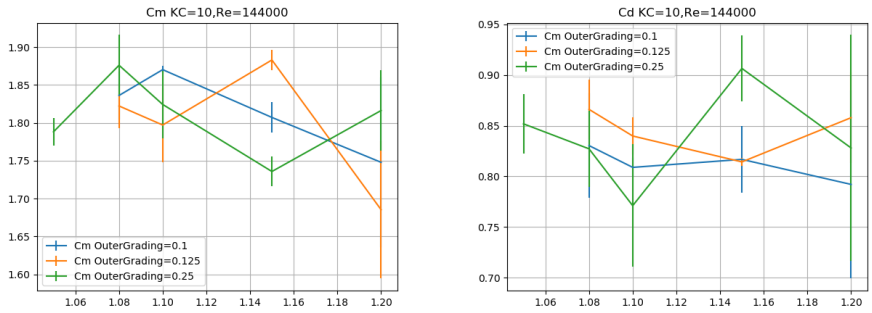

(a) **(b)**

Figure 5.1.4: Mesh convergence for KC=10.

For higher KC values the flow is inherently hard to solve. Experiments show great variation of results. The considerable scatter in experimental and CFD results indicate complicated physical phenomena occurring at higher KC values. This is partly why no mesh were completely accurate. However, based on the presented data we conclude that the mesh converges faster for an outer grading factor of 0.1. The inner grading-factor at 1.08 captures the flow features and forces quite well, and is computationally much lighter than 1.05. This is thus chosen as the preferred mesh.

5.1.0.1 Time Consumption

As can be seen from the Figure 5.1.5 and Figure 5.1.6 the computational load on refining the mesh is severe. Accuracy definitely comes at a computational cost. It is believed that the chosen mesh shows balance between computational efficiency and accuracy.

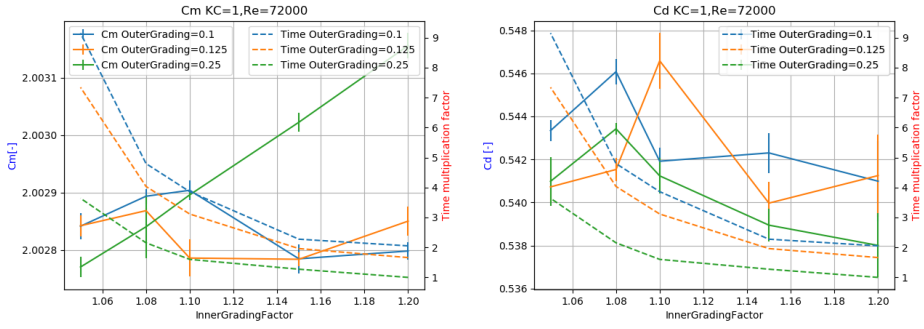

(a) **(b)**

Figure 5.1.5: Mesh convergence and computational time for KC=1

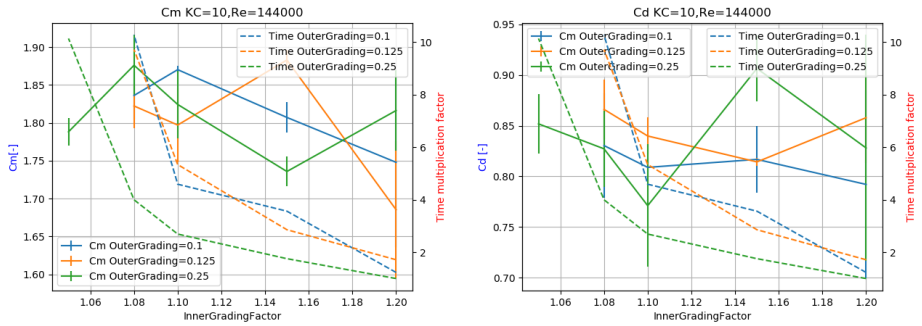

(a) **(b)**

Figure 5.1.6: Mesh convergence and computational time for KC=10

5.1.1 Domain Size

The domain size is affecting the flow field around the cylinder if it is not sufficiently large. By altering the domain size and testing for multiple KC numbers, the impact on the forces are investigated. The mesh inside the outer control circle is kept constant, and so is the cell size in the far field part of the domain. Increasing the domain size is obviously increasing the cell count within the domain, and thus making it computationally heavier. Theoretically, from potential theory, es the disturbance from a cylinder proportional to $\frac{1}{r^2}$, at a distance r from the cylinder. There is a variation as the size is altered, but a domain size of 20D showed to be fairly consistent with the larger 30D. To avoid the time-consuming larger domain, 20D was thus chosen as the final domain size.

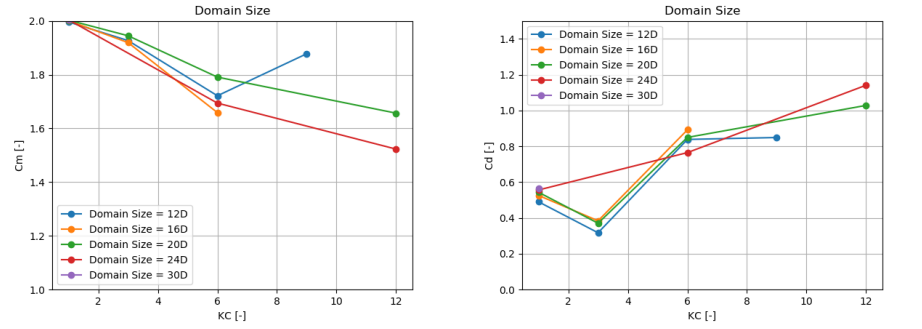

(a) **(b)**

Figure 5.1.7: Domain size convergence

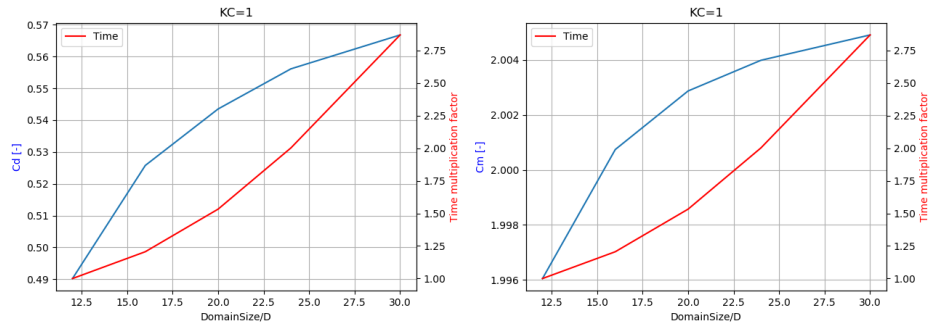

(a) **(b)**

Figure 5.1.8: Domain size and computational time

5.1.2 Courant Number Dependence

An investigation of the impact of the Courant number was done. For $Co < 1$ there was no clear trend in the results and they were consistent. For computational reasons a high Courant number is beneficial as it allows for higher time steps. A value of 0.8 was chosen to ensure all higher loads were captured, and to avoid instabilities at higher Courant numbers.

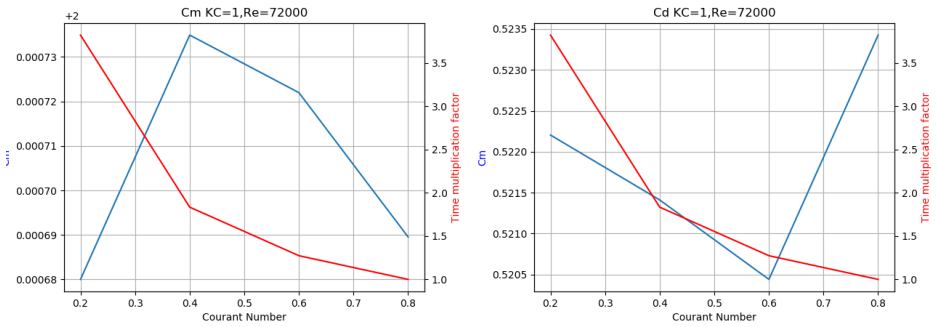

(a) **(b)**

Figure 5.1.9: Courant number dependencce

5.1.3 Number of Oscillation

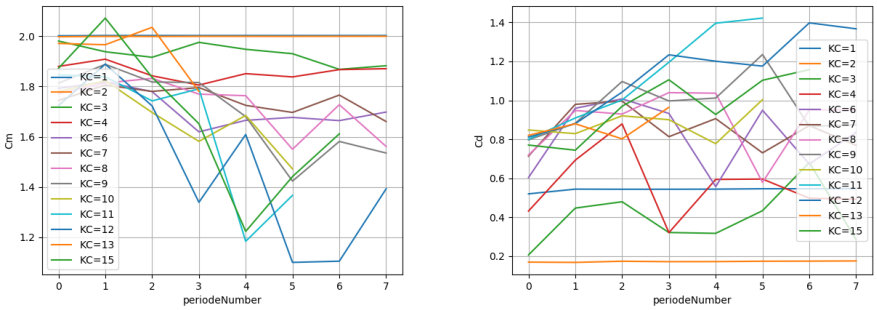

(a) **(b)**

Figure 5.1.10: Number of oscillations before quasi steady state

Observe that the forces for the lower KC numbers converge fast, and reach a steady state as early as after one or two oscillations. The steady state condition, if it exists, is not as pronounced for high KC numbers. The values oscillate severely. Due to computational limitations, a desire to keep the number of oscillations low arouse. It is also questionable whether a full steady state conditions could be found with the amount of vortices shedding, or if it is throughly unstable. Singh (1979) mentioned considerable variations was found between each cycle for high KC numbers. After five to six periods there is no clear trend, indicating that sort of convergence to a quasi steady state is reached. Ideally should averaging occur over many periods. However, the results indicate that 3 initialisation periods and averaging over five periods should be sufficient to get reliable results. One might however, expect slight deviation in the obtained results.

5.1.4 Core Convergence

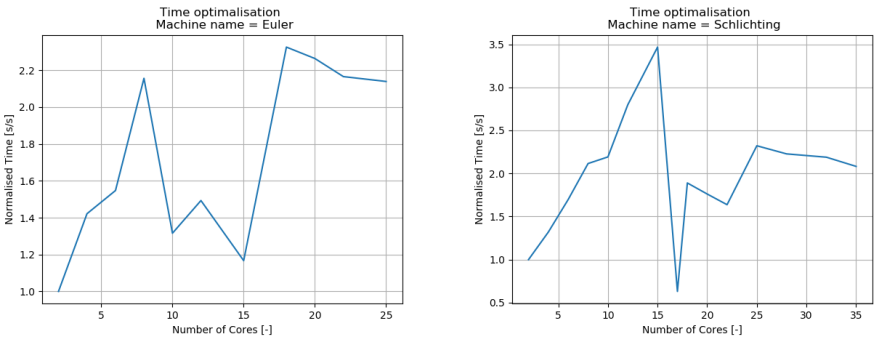

(a) **(b)**

Figure 5.1.11: Computational time vs number of cores for parallel runs

As time was a limiting factor, effort was put in ensuring maximum efficiency of the available computing power. As parallel computing was utilised, finding the optimum number of cores to solve the problem as efficient as possible was important. The final mesh was tested on a range of cores and then the time to preform the analysis was recorded. By normalising the time, (by the time for running on minimum amount of cores, as well as the number of possible parallel simulations on the computer), the optimum point for efficiently running multiple simulations were found. The optimum point would be the lowest total time consumption, and can be seen from Figure 5.1.11.

5.1.5 Final Mesh Quality

The final mesh has properties as defined in Table 5.1.1.

Mesh Quality		
Hexahedra cells = 283956		
Variabel	**Max**	**Average**
Aspect ratio	29.1595	-
Non Orthogonality	44.341	6.95782
skewness	0.524302	-
Variabel	**Value**	
Inner Grading Factor	1.08	
Outer Grading Factor	0.1	
Domain Size	20D	
Courant Number	0.8	

Table 5.1.1: Final mesh properites

A visualisation of key-points in the domain could be seen in Figure 5.1.13 and Figure 5.1.13:

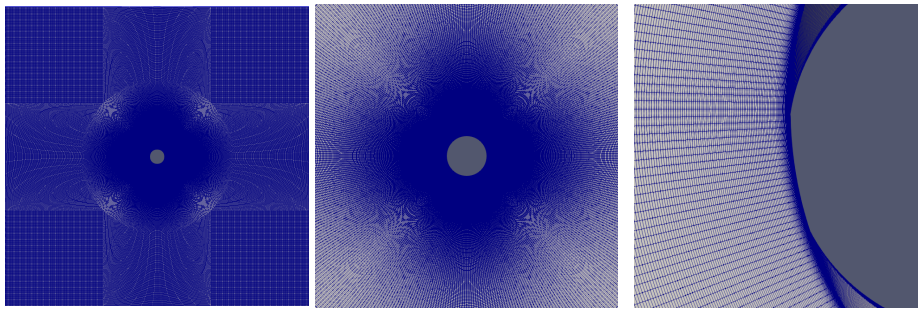

(a) **(b)** **(c)**

Figure 5.1.12: Full domain for the final mesh, distance 10r to each side and close to the cylinder to visualise the boundary layer

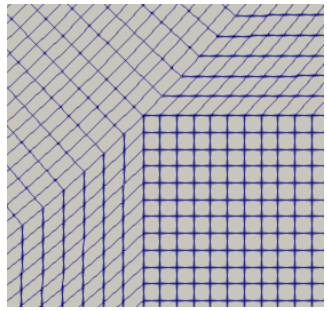

Figure 5.1.13: Outside the outer control circle where the cell size across boarders was kept constant.

5.2 Validation of Numerical Results

Throughout history several studies on circular cylinders in oscillating flow has been performed. It is a substantial amount of data available as grounds for comparison. It should be noted that the experiments show a high degree of scatter. The results obtained by CFD were compared to experimentally obtained results from Sarpkaya (1976a) and Bearman, Downie, et al. (1985). The results shows a fairly good agreement. It should be mentioned that for low KC numbers, C_M is a bit lower than experimental data, but follows the trend with a distinct drop at $KC \approx 6$. Singh (1979) discussed the considerable amount of scatter between different papers. He mentions that many might have been prone to experimental errors as simple, analoge apparatus for force sampling was used. However, the CFD setup obtain values within the natural scatter amongst experiments.
At $KC = 12$, a sudden drop in C_M accompanied by a spike in C_D, while at $KC = 14$ the opposite occurs.This seems a bit unlikely, even though experiments have shown variations, these are less distinct. The cause might be that the analysis was yet to reach steady state. It could also be observed that the standard deviations is quite large at this point, which indicates a time dependent variation.

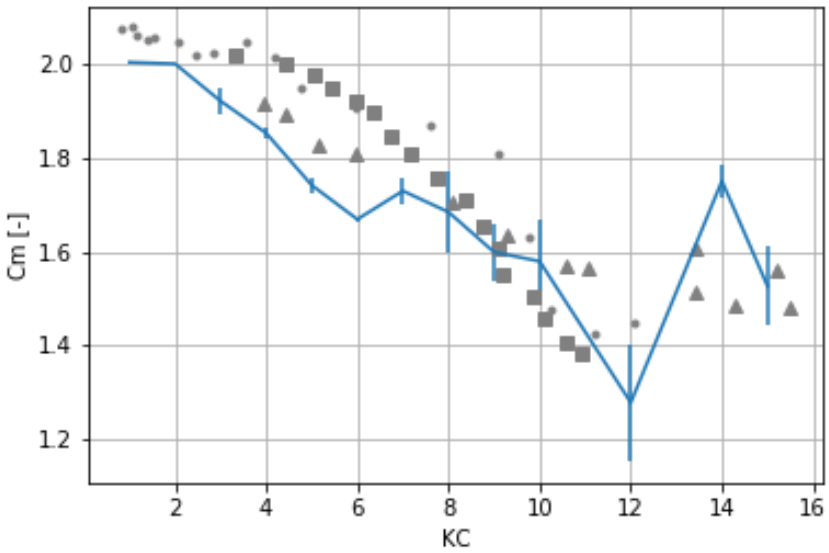

Figure 5.2.1: Comparison of C_M 2D CFD and experimental result, ■ Sarpkaya (1976a) $\beta = 11525$, ● Sarpkaya (1976a) Re=40 000, ▲ Bearman, Downie, et al. (1985)

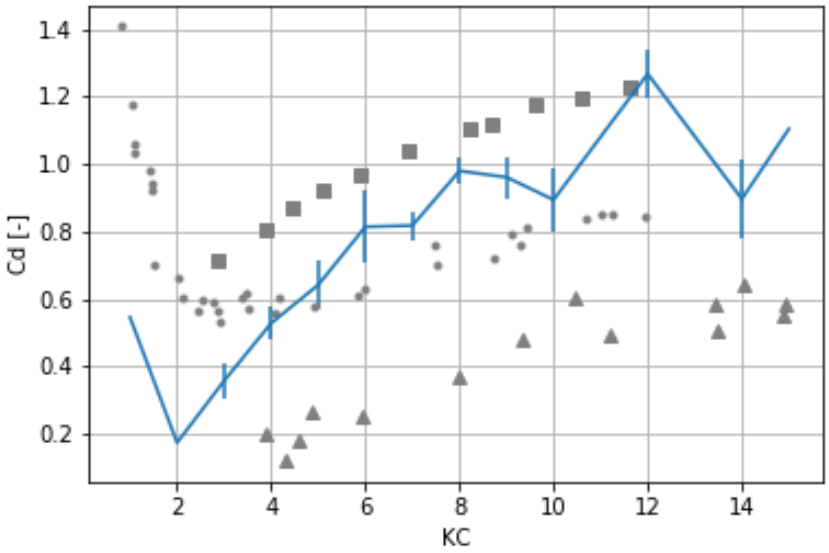

Figure 5.2.2: Comparison of C_D 2D CFD and experimental result,■ Sarpkaya (1976a) $\beta = 11525$,● Sarpkaya (1976a) Re=40 000, ▲ Bearman, Downie, et al. (1985)

5.3 3D Discretisation

The 3D problem is discretisised from a 3D problem to a 2D problem by the same analogy as strip theory. A Lagrangian style mesh is used, where the strips follow the vertical position of a water particle. The water oscillating the monopile will thus have the right disturbance levels, as it is the "same" water-particle and vortices which have shedded that reinteract with the cylinder. This will more accurately capture the physical phenomena occurring at each strip.

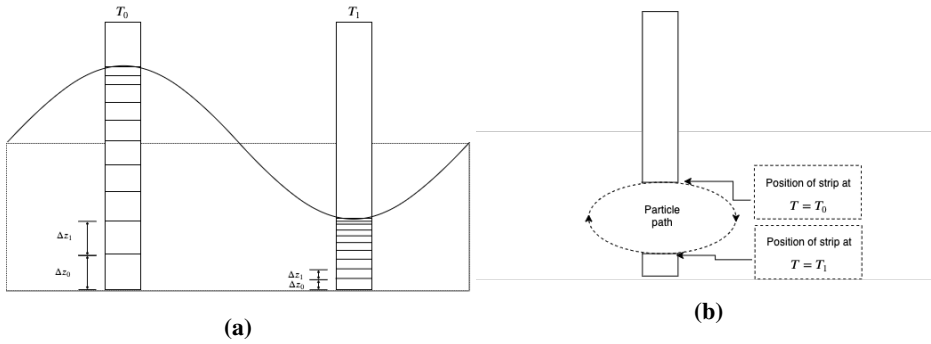

Figure 5.3.1: Strip position over one cycle compared to the particle path.

The strips are carefully placed so that the velocity change across each strip is the same. The region with high gradient at the top is resolved by more strips.

To obtain an estimate of the amount of strips necessary to accurately solve the problem the FNV theory was calculated with the number of strips ranging from 5 to 15 at the most severe sea state where $H_1/\lambda = 1/25$. Choosing a severe sea state results in a conservative discretisation. The results showed convergence at ten strips, and it is assumed that the expanded CFD-FNV theory follows roughly the same trend, indicating that ten strips should be sufficient.

This is thus chosen as the preferred discretisation.

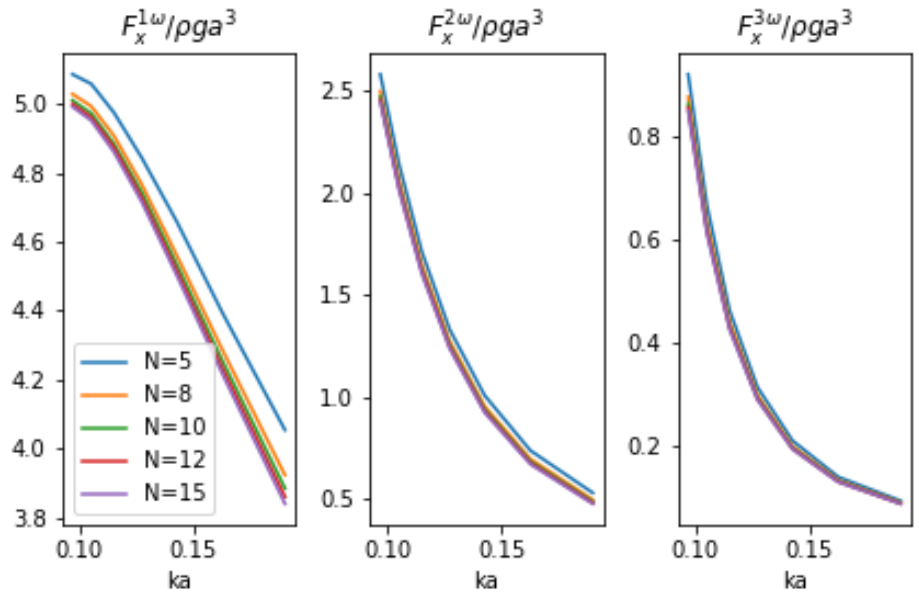

Figure 5.3.2: Number of strips necessary for accurate FNV calculations, $H_1/\lambda = 1/25$.

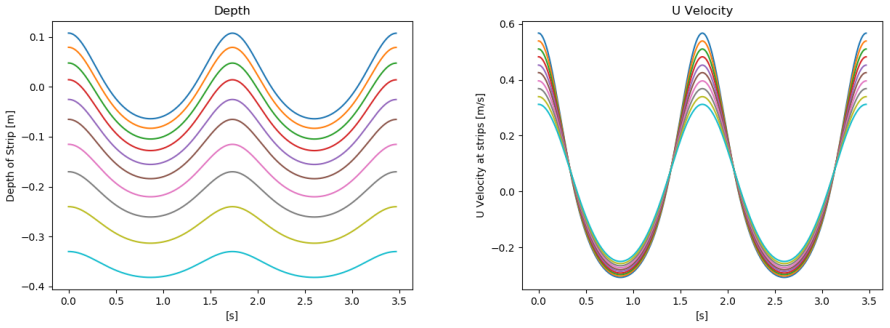

(a) **(b)**

Figure 5.3.3: Strip position and corresponding velocity.

In Figure 5.3.3, the depth of each strip, together with the velocity at the strip is presented. The colours used in the depth plot can be found in the velocity plot.

5.3.1 Examples of Wave Kinematics

An example of the wave kinematics calculated with Stokes fifth order wave theory is presented in Figure 5.3.4a and Figure 5.3.4b.

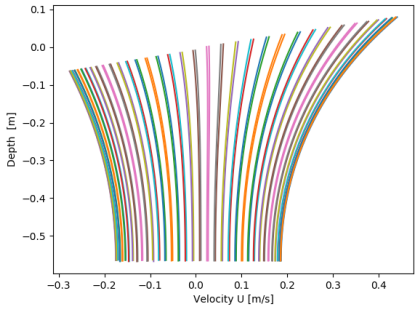

(a) U velocity - Stokes 5th order for wave periode 1 .4433 s and $H_1/\lambda = 20$,h=0.5625.

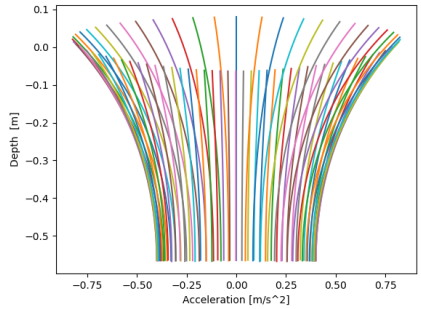

(b) U velocity - Stokes 5th order for wave periode 1 .4433s, and $H_1/\lambda = 20$,h=0.5625.

5.3.2 Derivative of Velocity Between Strips

To obtain the properties necessary to solve Equation 2.5.5 lines reaching out in the radial direction was put, in the domain. Each line contained 100 equidistant probes to sample the velocity at each time-step. A total of 180 lines meant each line covered $\Delta\theta = 2\,\mathrm{deg}$ (illustrated in Figure 5.3.5). The effect of changing these parameters was never tested as time limits made it impossible to conduct such thorough tests. They were thus chosen to be what was expected by the author to be sufficient. Increasing the amount of probes highly impacts the storage capacity required, as well as the complexity of post-processing as these files contained roughly 200 gigabytes to scan through for each wave condition.

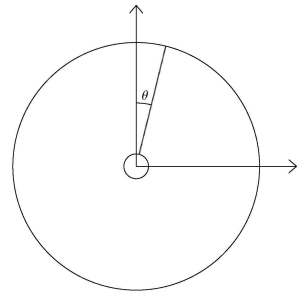

Figure 5.3.5: Probe positions in the domain.

5.4 Automation of OpenFOAM

To efficiently run the vast amount of analysis required to achieve accurate results, a python script was written to run the CFD simulations. This ensured all computational power was fully utilised. The script create a folder-structure for the analyses, calculates fifth order stoke waves as input, creates a mesh, applies the correct turbulence parameters and starts the calculation on the desired amount of cores. As soon as a calculation is finished the next one starts to avoid down time. The python interface ensures little human interaction to keep flaws away. When the python scripts were used, effort could be focused elsewhere making the CFD analysis an automated process. The script only relied on the input of the desired test conditions and mesh parameters previously derived. The same script were slightly altered and used for the mesh convergence test and showed reliable behaviour.

Chapter 6

Results

Throughout the process of obtaining the results, a vast amount of data was produced. The computational effort necessary to calculate a single wave condition limited the amount of different cases investigated. The expanded CFD-FNV theory was compared to results obtained by Kristiansen and Faltinsen (2017a), with focus on the third harmonics, as discrepancy between theory and experiments were substansial. A thorough investigation for the importance of the different terms will be shown.

6.1 Test Program

The test program was created to match the experiments done by Kristiansen and Faltinsen (2017a). As both computational and storage capacity was a limiting factor, the tests were limited to 4 periodes, namely $T = \{1.299s, 1.732s, 1.876s, 2.021s\}$. Each period was tested for steepness parameters $H_1/\lambda = \{1/25, 1/30, 1/40\}$. All for the water depth of 0.5625 m. The previously mentioned Ursell number is well below 40, indicating that Stokes fifth order theory is applicable.

6.2 FNV vs CFD-FNV

An example of the unfiltered signal obtained by CFD and CFD-FNV theory is shown in Figure 6.2.1. The FNV and FNV-CFD shows a good agreement of the total force.

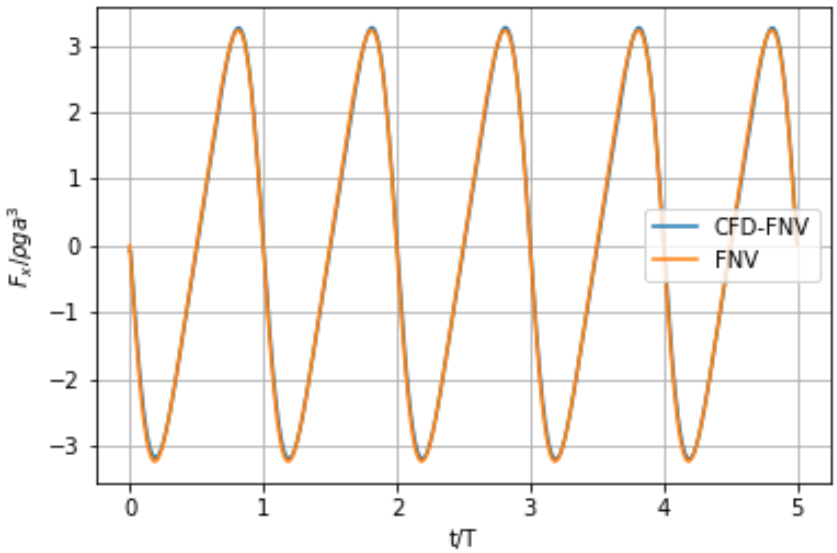

Figure 6.2.1: Unfiltered signal of the total force $F_x/\rho g a^3$ for $ka = 0.115$ and $H_1/\lambda = 1/40$.

By applying a bandpass filter, the difference in the higher order harmonics becomes more pronounced. The first and second harmonic load show remarkable resemblance, where the discrepancy occurs at the third harmonic. A slight end effect from the filter is observed Figure 6.2.4.

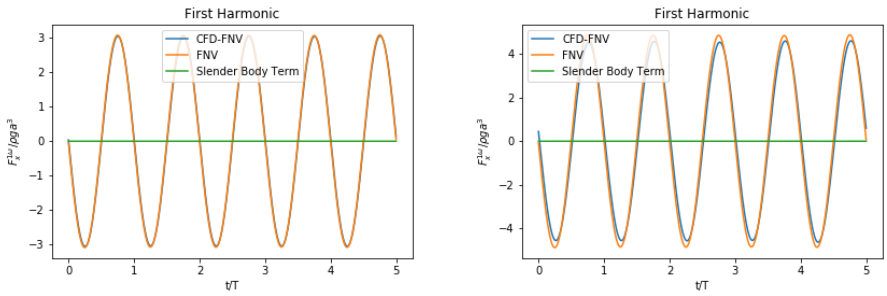

(a) **(b)**

Figure 6.2.2: First harmonic force $F_x/\rho g a^3$ for $ka = 0.115$ and $H_1/\lambda = 1/40$ and $H_1/\lambda = 1/25$ respectively.

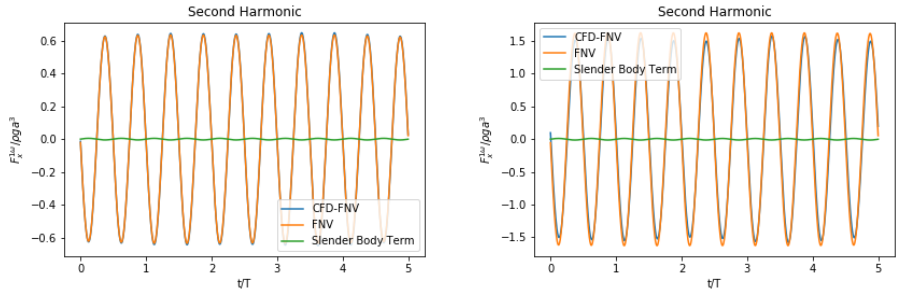

(a) **(b)**

Figure 6.2.3: Second harmonic force $F_x/\rho g a^3$ for $ka = 0.115$ and $H_1/\lambda = 1/40$ and $H_1/\lambda = 1/25$ respectively.

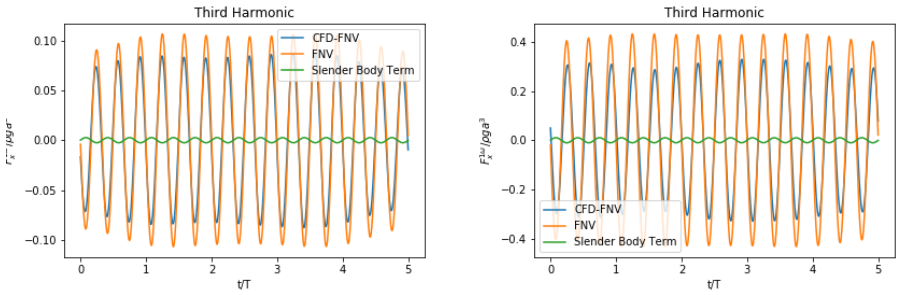

(a) **(b)**

Figure 6.2.4: Third harmonic force $F_x/\rho g a^3$ for $ka = 0.115$ and $H_1/\lambda = 1/40$ and $H_1/\lambda = 1/25$ respectively.

Observe that the slender body term has no effect on the first order forces. This is consistent with the good agreement between FNV theory and experiments previously discussed. There is a slight effect on the second harmonic load, but the real impact is on third harmonic. The extra force term is 180 degrees out of phase. The inclusion of viscous effects also slightly lowers the amplitude of the third harmonic force.

6.3 Comparison of the CFD-FNV Method to Experiments

The FNV theory and experiments generally predicts the same first and second harmonic loads for a broad range of conditions. However, for the third harmonic loading, the FNV theory over-predicts the loads for more severe sea states. As was shown in the experiments section.

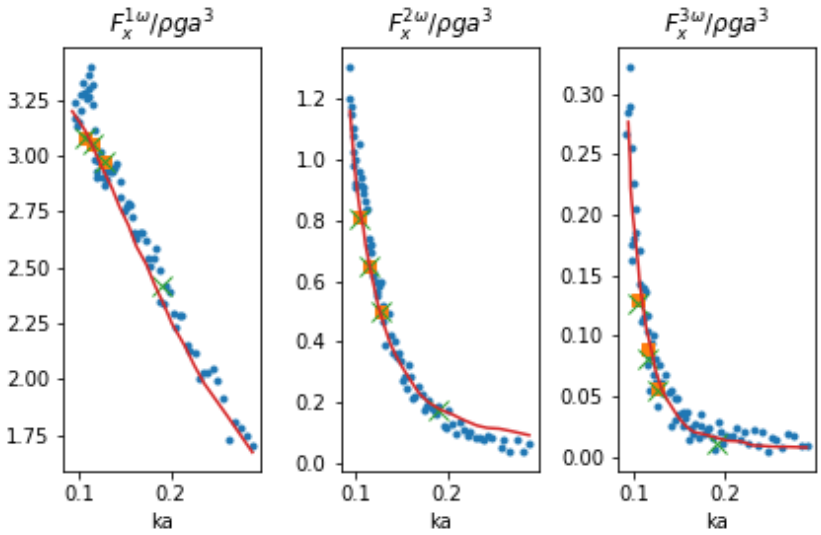

Figure 6.3.1: Non-dimensional force amplitudes for $H_1/\lambda = 1/40$, vs non dimensional wave-number ka, • Experiments by Kristiansen and Faltinsen (2017a), ■ CFD-FNV without slender body term, × CFD-FNV,– FNV.

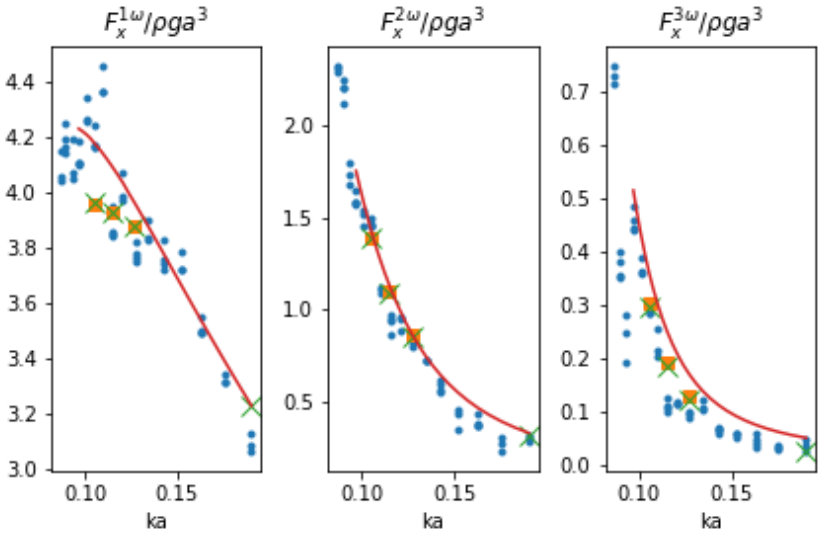

Figure 6.3.2: Non-dimensional force amplitudes for $H_1/\lambda = 1/30$, vs non dimensional wave-number ka, • Experiments by Kristiansen and Faltinsen (2017a), ■ CFD-FNV without slender body term, × CFD-FNV,– FNV.

For $H_1/\lambda = 1/40$, both the FNV and CFD-FNV theory predicts the loads very well.

There is no discrepancy between the results. For the third harmonic, the CFD-FNV predicts a lower value than the FNV, but is still consistent with the lower values of experimental results.
For $H_1/\lambda = 1/30$, the discrepancy between the FNV theory and experiments becomes quite pronounced. For the third harmonic, the CFD-FNV method predicts values that are consistent, though slightly higher than experimental results. The CFD-FNV method predicts lower forces than the FNV theory in regards to first harmonic. For lower ka numbers, there is quite a bit of variation in the experimental results. The CFD-FNV theory seems to predict a low value, but within the natural differences of the experimental data.

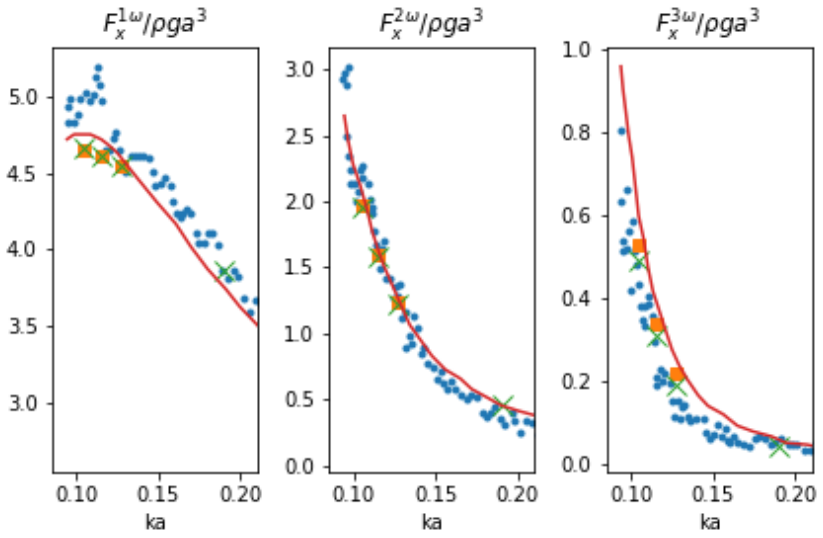

Figure 6.3.3: Non-dimensional force amplitudes for $H_1/\lambda = 1/25$, vs non dimensional wavenumber ka, • Experiments by Kristiansen and Faltinsen (2017a), ■ CFD-FNV without slender body term, × CFD-FNV,– FNV.

$H_1/\lambda = 1/25$ is the point where the discrepancy between experiments and FNV theory was discussed by Kristiansen and Faltinsen (2017a). The estimation of the third harmonic by CFD-FNV is closer to the experimental data. However, there is still a slight discrepancy.

With regards to the first harmonic the CFD-FNV method predicts lower first harmonic load for lower ka numbers, and seems to be more consistent for higher values where the match compared to experimental data is perfect. It is worth mentioning that the second order loads are consistent for both FNV and CFD-FNV with regards to experiments.
The model seems to more accurately model the third harmonic, but as the FNV model it under-predicts the first harmonic load for the most severe sea states. The difference between the original FNV theory and experiments is partially described by the inclusion of 2D viscous effects and the 3D expansion. Both contributes to better compliance with experimental data.

6.3.1 Dependence on KC_5

The different harmonics and their dependency on the wave number k were investigated as done by Kristiansen and Faltinsen (2017a). Additionally the dependence on other parameters such as Reynolds number, KC number etc were investigated. As the KC number originally is defined for a sinusoidal oscillating flow, we introduce a new parameter to describe the in the same manner, by using the maximum horizontal velocity from Stokes 5th order theory

$$\mathrm{KC}_5 = \frac{U_{m5}T}{D}. \tag{6.3.1}$$

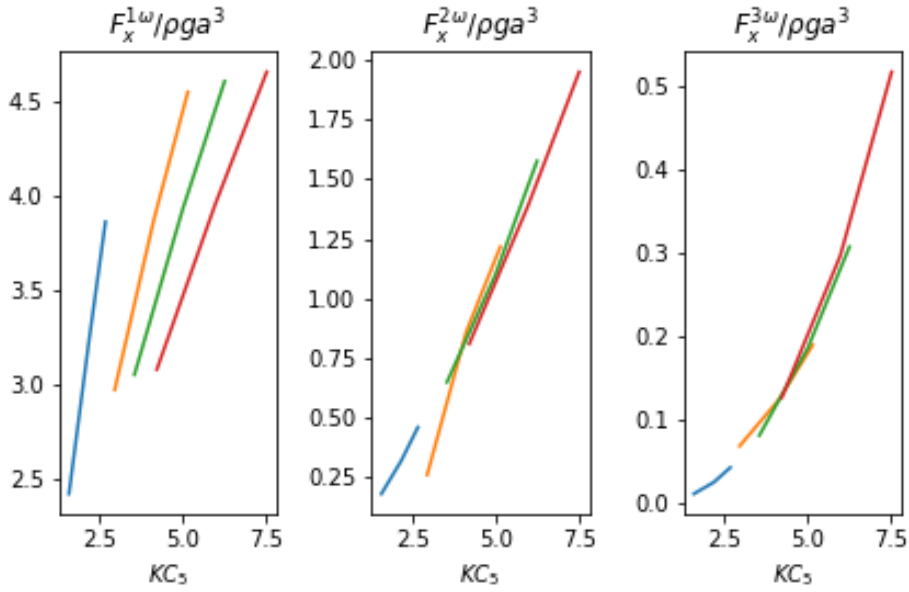

Figure 6.3.4: Non-dimensional force amplitudes vs KC Number, — T=2.021, — T=1.876, — T=1.732, — T=1.299 CFD-FNV.

From Figure 6.3.4, we observe that the second and third harmonic loads seem to be a function of KC number, whereas the first harmonic shows less KC dependence. It is believed that the higher order loads is dependent on vortex shedding, and thus is the importance of KC high for these loads.

It should be mentioned that the number of results are fairly low, and too low to make a generalisation, but it is believed that they indicate important phenomena. Experimental results were overlaid to confirm the hypothesis. They could be seen in section A.3. The experimental results indicate that the second harmonic is proportional to the KC numbers, whereas a lot more scatter was found surrounding the third harmonic. The trend could thus be a result of numerics, or a coincidence due to the low amount of data points. In section A.3, the dependence on Reynolds number is also shown. There is a clear trend that

by increasing the Reynolds number the forces increase. This could be due to the simple fact that a higher Reynolds number means more severe sea state. Whether the effect is directly connected to the Reynolds number is questionable.

6.4 Vorticity Field

The vorticity around the cylinder was visualised. The visualisation is taken for the 8th oscillation at the free surface of the wave. The smoothening effect of RANS is observed, but the method is fully capable of capturing the larger vortices, as small vortex concentrations is not fully resolved. A similar figure for $H_1/\lambda = 1/40$, T=1.73 can be found in section A.4.

(a) t=0T **(b)** t=0.2T

Figure 6.4.1: Vorticity at the surface for $H_1/\lambda = 1/25$, T=1.73.

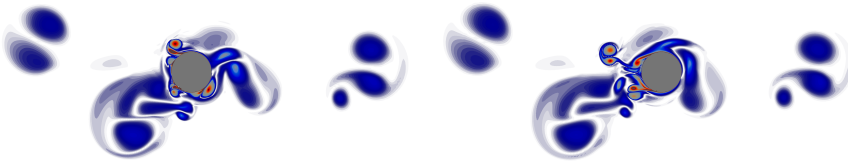

(a) t=0.4T **(b)** t=0.6T

Figure 6.4.2: Vorticity at the surface for $H_1/\lambda = 1/25$, T=1.73.

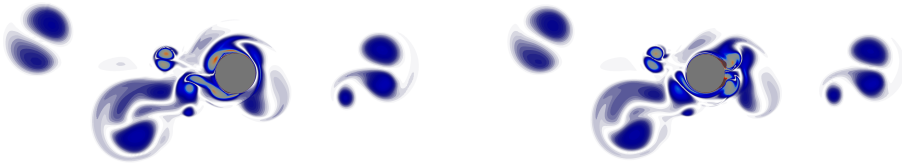

(a) t=0.8T **(b)** t=T

Figure 6.4.3: Vorticity at the surface for $H_1/\lambda = 1/25$, T=1.73s.

The scenario tested in the experiments, and shown in Figure 3.2.3, was recreated in CFD with the purpose of visual comparison. The vortices, which are believed to cause the upwash, is depicted in Figure 6.4.4. The CFD analysis is taken at the surface and should be a direct replica of the conditions tested in the tank. Observe the smoothening caused by the averaging in the RANS method, but the similarities are astonishing. The two vortices are separated by a small gap where the vortices are believed to induce velocities in 3D, leading to the observed water rise-up.

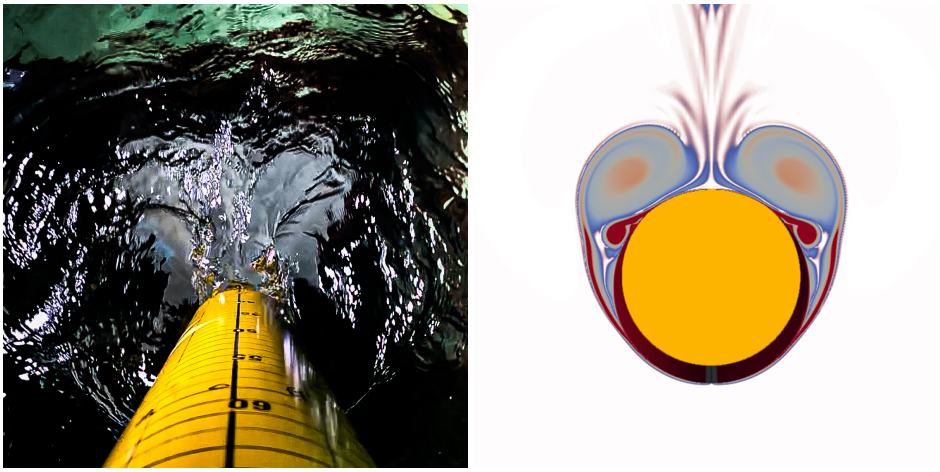

(a) **(b)**

Figure 6.4.4: Visual comparison of experimental vs numerical flow field (vorticity) for T=2.165 s,$H_1/\lambda = 1/25$.

Similar figures for an entire period is shown in section A.5.

6.4.1 Visualisation of Strip positioning

All analysis presented in this thesis have consisted of a total of ten strips discretising the cylinder, from 3D to multiple 2D domains. Calculations have been performed in the 2D domain before the solution was integrated back to a 3D solution. This was visualised by showing the vorticity field from each 2D strip in the 3D configuration which they occur.

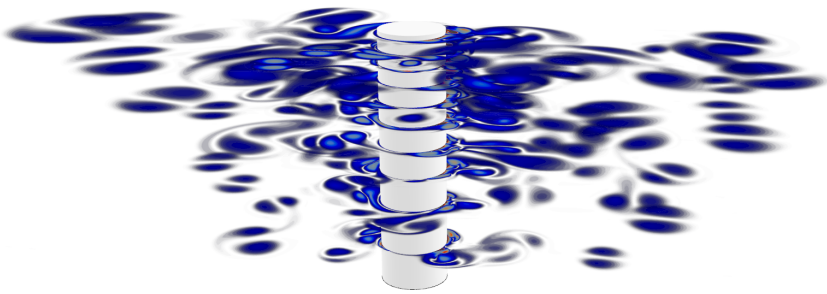

Figure 6.4.5: Super imposed vorticity field from 2D CFD below the wave crest, for $H_1/\lambda = 1/25$ and T=1.73s, seen from the side/behind and above the seabed.

Observe that as each strip is solved independently without information transfer, the vortex sheet develops independently. Hence is the vortex sheet not entirely representing the physical reality as the vortices might affect each other to force a pattern running along the cylinder. However, by examining the backside of the cylinder, the vortices seems to be consistent. It should also be noted that the visualisation confirms the assumption that the vortex strength is higher close to the surface.

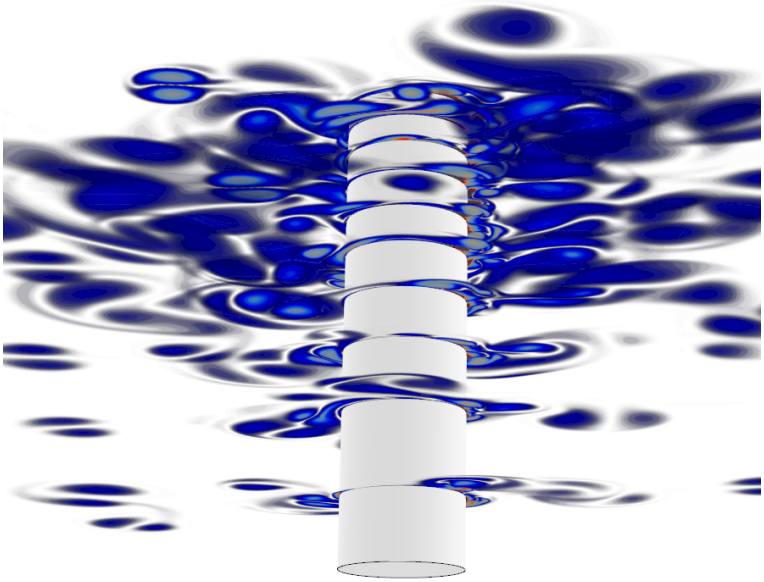

Figure 6.4.6: Super imposed vorticity field from 2D CFD below the wave crest, for $H_1/\lambda = 1/25$ and T=1.73s, seen from behind and below the seabed.

Similar figures for different angles as well as the 2D strips, can be found in section A.6.

Chapter 7

Discussion and Conclusion

In this master thesis a method for computing the harmonic wave loading on a surfacepiercing cylinder was derived. Numerical tools were used in combination with potential theory to create a combined CFD-FNV theory. The CFD model in OpenFOAM was tested on a sinusoidal flow and validated against experiments. The CFD model showed agreement for a broad range of conditions and generally obtained reliable results. An expansion term to 2D CFD analysis was included, in the hopes of improving the accuracy of the calculation by including additional force components as a semi 3D solution. The expansion term resulted in a force with a 3ω frequency when applied to stokes fifth order waves.

A 3D discretisation using a Lagrangian grid to accurately capture the backflow of vortices and ensure realistic flow condition was designed and implemented in the CFD-FNV method. The total CFD-FNV method was compared against experimental data from Kristiansen and Faltinsen (2017a), focusing on the third harmonic load. Kristiansen and Faltinsen (2017a) showed that a discrepancy in the FNV theory caused an over prediction of the third harmonic loads. By inclusion of viscous effects, and the previous mentioned slender body term, the CFD-FNV theory showed significant improvements in regards to the third harmonic loads compared to the the regular FNV theory. There is still a discrepancy in the results for the most severe sea states. During experiments, significant 3D effects was observed, which is not described by the incident velocity potential. The results show that a slender body assumption improves the estimation of third harmonic. However, as it still exist a discrepancy, the body's impact on flow probably should be included. The effect is best captured by 3D CFD, but could possibly be estimated and included in the potential for incident flow to improve the accuracy of the proposed procedure.

The second and third harmonic loads obtained from CFD was dependent on the KC number. When the experimental data from Kristiansen and Faltinsen (2017a) was overlaid, the same result showed for the second harmonic. The third harmonic had greater variation and scatter.
There is still work to be done on this topic to improve and validate the tools created during this thesis. A continuation on the work regarding the lifting-line theory to describe the upwell and further include the 3D effects in the Navier Stokes expansion should be done.

The visual comparison showed remarkable compliance, so this is an interesting field of study for further works. There are parameters whose impact on the results never were investigated, such as the number of CFD strips necessary. This should also be confirmed if further work was to be carried out.

Chapter 8

Bibliography

(PDF) Regions of Validity of Analytical Wave Theories (2019). URL: https://www.researchgate.net/publication/250074153_Regions_of_validity_of_analytical_wave_theories (visited on 12/14/2019).

A Fifth-Order Stokes Theory for Steady Waves | Journal of Waterway, Port, Coastal, and Ocean Engineering | Vol 111, No 2 (2019). URL: https://ascelibrary.org/doi/abs/10.1061/%28ASCE%290733-950X%281985%29111%3A2%28216%29 (visited on 12/14/2019).

Bachynski, E. E., Kristiansen, T., and Thys, M. (2017a) Experimental and Numerical Investigations of Monopile Ringing in Irregular Finite-Depth Water Waves. In: *Applied Ocean Research*byeditor+others, pp. 154–170. ISSN: 0141-1187. DOI: 10.1016/j.apor.2017.08.011.

— (Oct. 1, 2017b) Experimental and Numerical Investigations of Monopile Ringing in Irregular Finite-Depth Water Waves. In: *Applied Ocean Research*byeditor+others, pp. 154–170. ISSN: 0141-1187. DOI: 10.1016/j.apor.2017.08.011.

Bearman, P. W. and Chaplin, J. R. (1985/00/00) THE LOADING ON A CYLINDER IN POST-CRITICAL FLOW BENEATH PERIODIC AND RANDOM WAVES. In: byeditor+others.

Bearman, P. W., Chaplin, J. R., Graham, J. G., Kostense, J. K., and Klopman, G. (July 1985) "The Loading on a Cylinder in Post-Critical Flow beneath Periodic and Random Waves." conference. 4th International Conference on Behaviour of Offshore Structures.

Bearman, P. W., Downie, M. J., Graham, J. M. R., and Obasaju, E. D. (May 1985) Forces on Cylinders in Viscous Oscillatory Flow at Low Keulegan-Carpenter Numbers. In: *Journal of Fluid Mechanics*byeditor+others, pp. 337–356. ISSN: 1469-7645, 0022-1120. DOI: 10.1017/S0022112085001562.

Bearman, P. W., Obasaju, E. D., and Graham, J. M. R. (Nov. 1988) A Study of Forces, Circulation and Vortex Patterns around a Circular Cylinder in Oscillating Flow. In: *Journal of Fluid Mechanics*byeditor+others, pp. 467–494. ISSN: 1469-7645, 0022-1120. DOI: 10.1017/S0022112088002782.

Brorsen, M. (2007) Non-Linear Waves. In: *Department of Civil Engineering*. Aalborg University.

Chaplin, J. R., Rainey, R. C. T., and Yemm, R. W. (Nov. 1997) Ringing of a Vertical Cylinder in Waves. In:
*Journal of Fluid Mechanics*byeditor+others, pp. 119–147. ISSN: 1469-7645, 0022-1120. DOI: 10.1017/S002211209700699X.

Courant, R., Friedrichs, K., and Lewy, H. (Mar. 1967) On the Partial Difference Equations of Mathematical Physics. In:
*IBM Journal of Research and Development*byeditor+others, pp. 215–234. ISSN: 0018-8646. DOI: 10.1147/rd.112.0215.

Faltinsen, O. M. (Feb. 1, 1999) Ringing Loads on a Slender Vertical Cylinder of General Cross- Section. In:
*Journal of Engineering Mathematics*byeditor+others, pp. 199–217. ISSN: 1573-2703. DOI: 10.1023/A:1004362827262.

Faltinsen, O. M., Newman, J. N., and Vinje, T. (Apr. 1995) Nonlinear Wave Loads on a Slender Vertical Cylinder. In:
*Journal of Fluid Mechanics*byeditor+others, pp. 179–198. ISSN: 1469-7645, 0022-1120. DOI: 10.1017/S0022112095001297.

Faltinsen, O. M. (1990a) *Sea Loads on Ships and Offshore Structures*. Cambridge Ocean Technology Series. Cambridge: University Press. viii+328. ISBN: 978-0-521-37285-5.

— (1990b) *Sea Loads on Ships and Offshore Structures*. Cambridge Ocean Technology Series. Cambridge: University Press. 15 pp. ISBN: 978-0-521-37285-5.

Fenton John D. (Mar. 1, 1985) A Fifth-Order Stokes Theory for Steady Waves. In:
*Journal of Waterway, Port, Coastal, and Ocean Engineering*byeditor+others, pp. 216–234. DOI: 10.1061/(ASCE)0733-950X(1985)111:2(216).

Fimland, D. H. a. (2018) Nonlinear Wave Loads on a Vertical Cylinder. In:

Griffin, R. (2020) On Vortex Strength and Drag in Bluff-Body Wakes. In:
*Journal of Fluid Mechanics*byeditor+others.

Guerrero, J. (n.d.) *Discretization Schemes – How to Choose the Schemes*.

H. K. Versteeg (2007) *An Introduction to Computational Fluid Dynamics: The Finite Volume Method*. In collab. with W. Malalasekera. 2nd ed. Harlow: Pearson/Prentice Hall, pp. XII, 503. xii+503. ISBN: 978-0-13-127498-3.

H. K. Versteeg and W. Malalasekera (2020) *An Introduction to Computational Fluid Dynamics: The Finite Volume Method*. 3rd ed. Prentice Hall/Pearson Education. ISBN: 978-0-273-73805-3.

Hedges, T. (Jan. 6, 1995) Regions of Validity of Analytical Wave Theories. In:
*Proceedings of The Ice - Water Maritime and Energy*byeditor+others, pp. 111–114. DOI: 10.1680/iwtme.1995.27656.

Holzmann, T. (Nov. 3, 2019) *Mathematics, Numerics, Derivations and OpenFOAM®*. DOI: 10.13140/RG.2.2.27193.36960.

Ibrahim, M. and Hashim, W. (Jan. 1994) Oscillating Flow in Channels with a Sudden Change in Cross Section. In:
*Computers & Fluids*byeditor+others, pp. 211–224. ISSN: 00457930. DOI: 10.1016/0045-7930(94)90035-3.

Keulegan, G. and Carpenter, L. (May 1958) Forces on Cylinders and Plates in an Oscillating Fluid. In:

*Journal of Research of the National Bureau of Standards*byeditor+others, p. 423. ISSN: 0091-0635. DOI: 10.6028/jres.060.043.

Kristiansen, T. and Faltinsen, O. M. (Dec. 2017a) Higher Harmonic Wave Loads on a Vertical Cylinder in Finite Water Depth. In:
*Journal of Fluid Mechanics*byeditor+others, pp. 773–805. ISSN: 0022-1120, 1469-7645. DOI: 10.1017/jfm.2017.702.

— (Dec. 2017b) Higher Harmonic Wave Loads on a Vertical Cylinder in Finite Water Depth. In:
*Journal of Fluid Mechanics*byeditor+others, pp. 773–805. ISSN: 0022-1120, 1469-7645. DOI: 10.1017/jfm.2017.702.

Langley Research Center, N. (n.d.) "Turbulence Modeling Resource."

LeBlond, P. H. and Mysak, L. A. (Jan. 1, 1981) *Waves in the Ocean*. Elsevier. 617 pp. ISBN: 978-0-08-087977-2. Google Books: TYGIwzz_k8kC.

Maccamy, R. C. and Fuchs, R. A. (1954) WAVE FORCES ON PILES: A DIFFRACTION THEORY. In:

Malenica, Š. and Molin, B. (Nov. 1995a) Third-Harmonic Wave Diffraction by a Vertical Cylinder. In:
*Journal of Fluid Mechanics*byeditor+others, pp. 203–229. ISSN: 1469-7645, 0022-1120. DOI: 10.1017/S0022112095004071.

— (Nov. 1995b) Third-Harmonic Wave Diffraction by a Vertical Cylinder. In:
*Journal of Fluid Mechanics*byeditor+others, pp. 203–229. ISSN: 1469-7645, 0022-1120. DOI: 10.1017/S0022112095004071.

Menter, F. R. (Aug. 8, 1994) Two-Equation Eddy-Viscosity Turbulence Models for Engineering Applications, in:
*AIAA Journal*byeditor+others, pp. 1598–1605.

Moukalled, F., Mangani, L., and Darwish, M. (2016) *The Finite Volume Method in Computational Fluid Dynamics: An Advanced Introduction with OpenFOAM® and Matlab*. Fluid Mechanics and Its Applications. Springer International Publishing. ISBN: 978-3-319-16873-9. DOI: 10.1007/978-3-319-16874-6.

Pettersen, B. (2007) *TMR 4247, Marin Teknikk 3, Hydrodynamikk*. Department Of Marine Technology.

Pope, S. B. (2000) *Turbulent Flows*. Cambridge: Cambridge University Press. ISBN: 978-0-521-59886-6. DOI: 10.1017/CBO9780511840531.

Rightslink® by Copyright Clearance Center (2019). URL: https://s100.copyright.com/AppDispatchServlet?publisherName=CUP&publication=FLM&title=Force%20on%20a%20circular%20cylinder%20in%20viscous%20oscillatory%20flow%20at%20low%20Keulegan%E2%80%94Carpenter%20numbers&publicationDate=2006-04-21&author=Turgut%20Sarpkaya&copyright=%C2%A9%201986%20Cambridge%20University%20Press&contentID=10.1017/S0022112086002999&startPage=61&endPage=71&orderBeanReset=True&volumeNum=165&issueNum=undefined (visited on 11/30/2019).

Sæter, T. (2019) Ringing Loads on Offshore Wind Turbine Monopiles. In:
byeditor+others.

Salim, S. M. and Cheah, S. C. (2009) Wall Y+ Strategy for Dealing with Wall-Bounded Turbulent Flows. In:
*Hong Kong*byeditor+others, p. 6.

Sarode, K., Naik, R., Jagtap, S., Pachpor, A., and Bansode, V. H. (2017) Benchmarking of Open FOAM for CFD Applications. In:
byeditor+others, p. 7.

Sarpkaya, T. (Jan. 29, 1976a) FORCES ON ROUGH-WALLED CIRCULAR CYLINDERS. In:
*Coastal Engineering Proceedings*byeditor+others, pp. 134–134. ISSN: 2156-1028. DOI: 10.9753/icce.v15.134.

— (Feb. 2, 1976b) Vortex Shedding and Resistance in Harmonic Flow about Smooth and Rough Circular Cylinders at High Reynolds Numbers. NPS-59SL76021. NAVAL POSTGRADUATE SCHOOL MONTEREY CA.

Schlisting, H. (1968) *Boundary-Layer-Theory*. 6th ed.

Singh, S. (1979) *Forces on Bodies in an Oscillatory Flow*. London: Department of Aeronautics, Imperial College, University of London.

Skjelberia, L. and Hendrickson, J. (1960) "Fifth Order Graity Wave Theory." In: *Costal Engineering*.

Sorensen, R. (Sept. 30, 1997) *Basic Coastal Engineering*. Springer Science & Business Media. 320 pp. ISBN: 978-0-412-12341-2. Google Books: PafNyKSg4EkC.

The Finite Volume Method in Computational Fluid Dynamics - An Advanced Introduction with OpenFOAM® and Matlab | F. Moukalled | Springer (2020). URL: https://www.springer.com/gp/book/9783319168739 (visited on 06/07/2020).

The Force Exerted by Surface Waves on Piles - OnePetro (2019). URL: https://www.onepetro.org/journal-paper/SPE-950149-G (visited on 11/30/2019).

Ursell, F. (Oct. 1, 1953) The Long-Wave Paradox in the Theory of Gravity Waves. In:
*Mathematical Proceedings of the Cambridge Philosophical Society*byeditor+others, pp. 685–694. DOI: 10.1017/S0305004100028887.

Wasserman, S. (n.d.) *Turbulence Models Offered by CFD Simulation Vendors*. ENGINEERING.com.

Appendix A

Appendix

A.1 Convergence Results

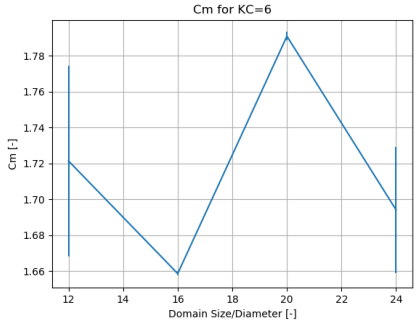

(a)

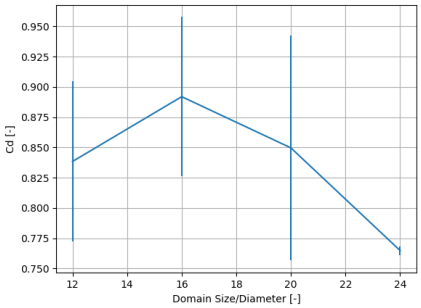

(b)

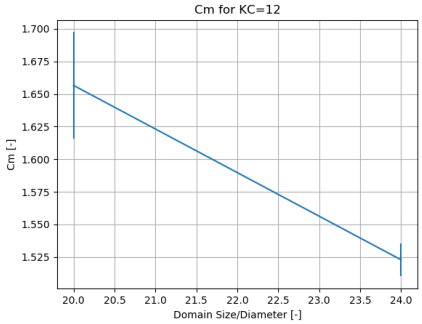

(a)

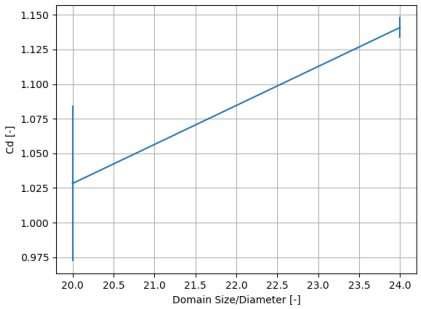

(b)

A.2 Experiments

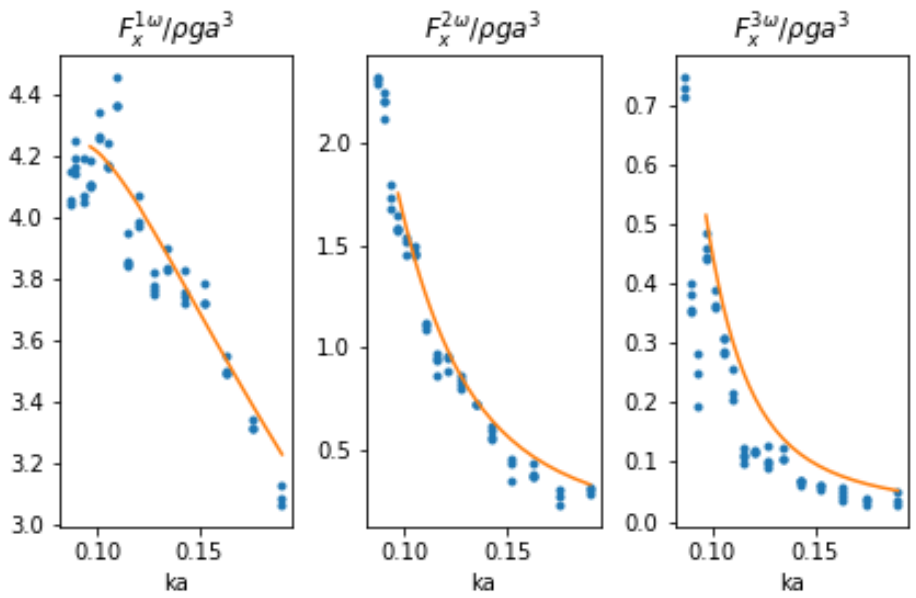

Figure A.2.1: First three force harmonics from Experiments (•), FNV theory (−) for $H_1/\lambda = 1/30$

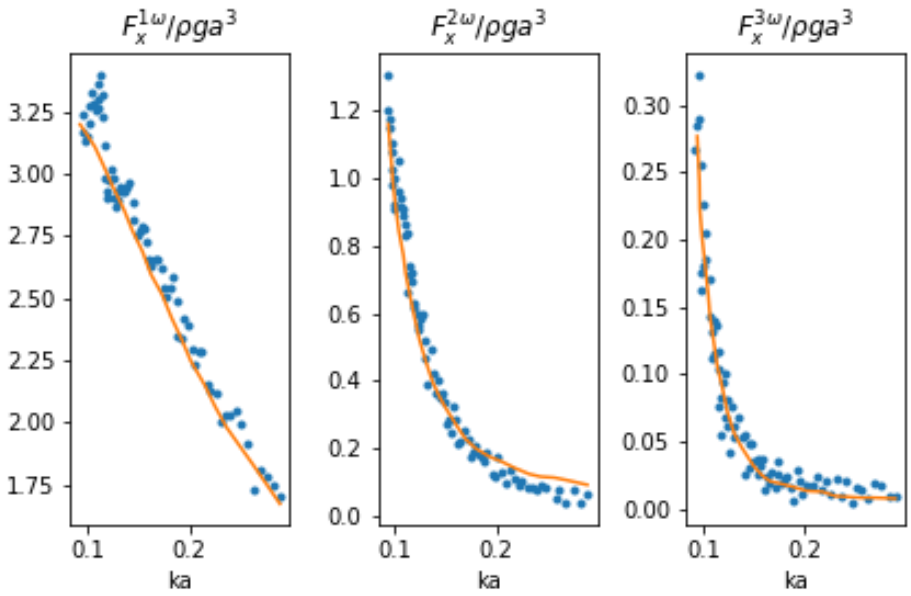

Figure A.2.2: First three force harmonics from Experiments (•), FNV theory (−) for $H_1/\lambda = 1/40$

A.3 Additional Results

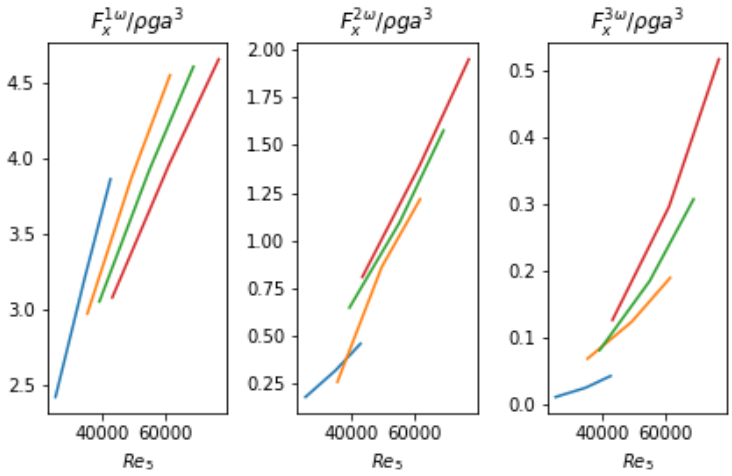

Figure A.3.1: Figure

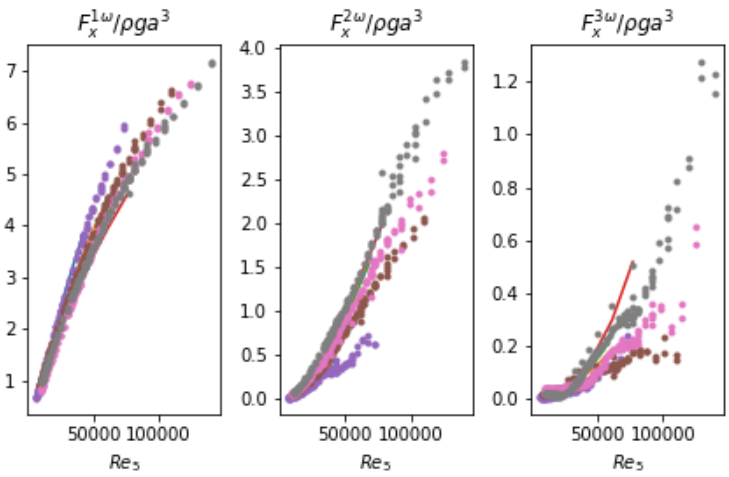

Figure A.3.2: Figure

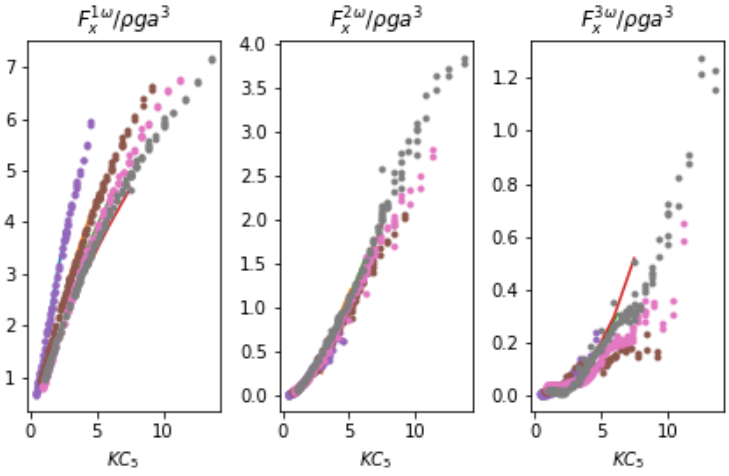

Figure A.3.3: Figure

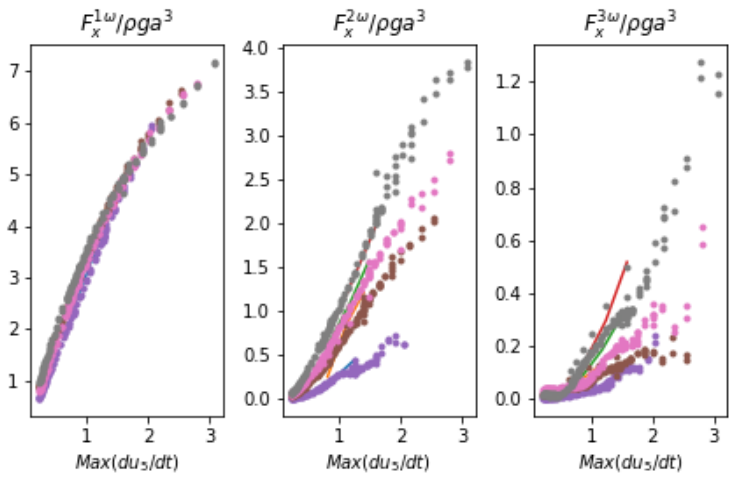

Figure A.3.4: Figure

A.4 Vorticity Field Over One Full Period

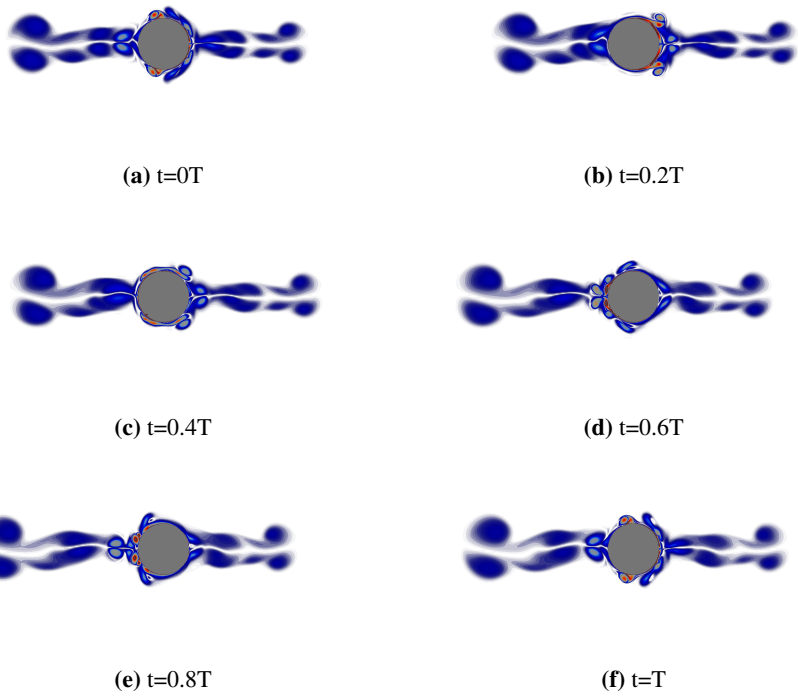

(a) t=0T **(b)** t=0.2T

(c) t=0.4T **(d)** t=0.6T

(e) t=0.8T **(f)** t=T

Figure A.4.1: Vorticity at the surface for $H_1/\lambda = 1/40$, T=1.73

A.5 Vorticity Comparison to Experimental Data

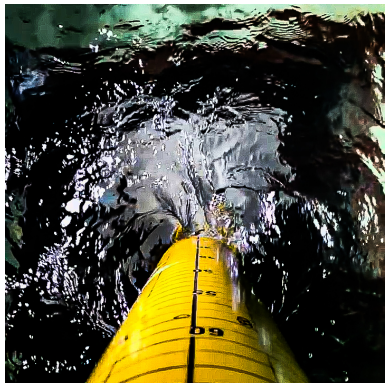

(a) t=0T

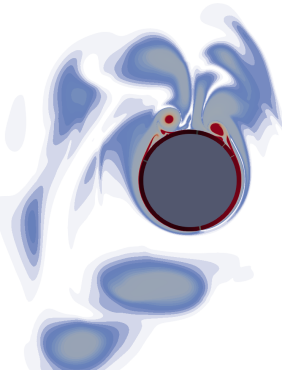

(b) t=0T

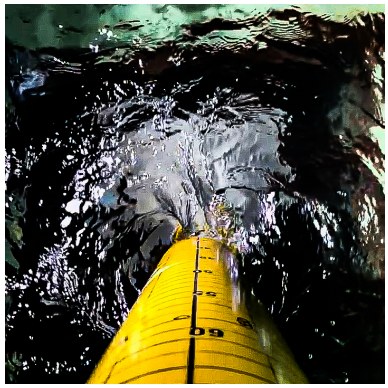

(c) t=0.1T

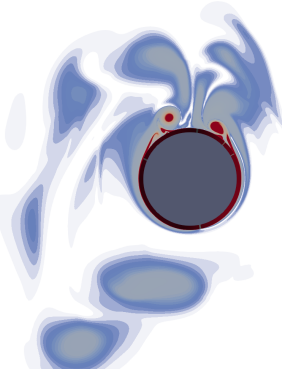

(d) t=0.1T

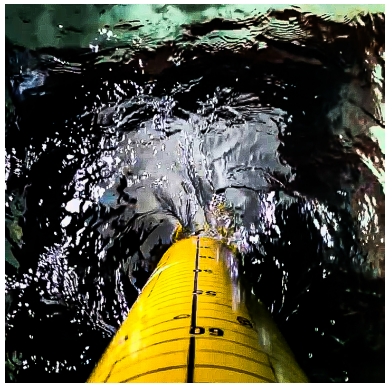

(e) t=0.2T

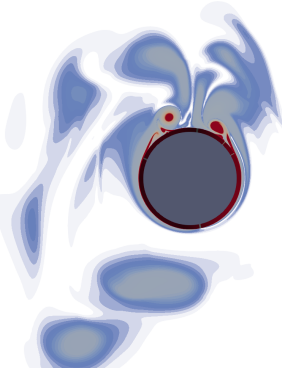

(f) t=0.2T

Figure A.5.1: Visual comparison of experimental vs numerical flow field (vorticity) for T=2.165 s,$H_1/\lambda = 1/25$.

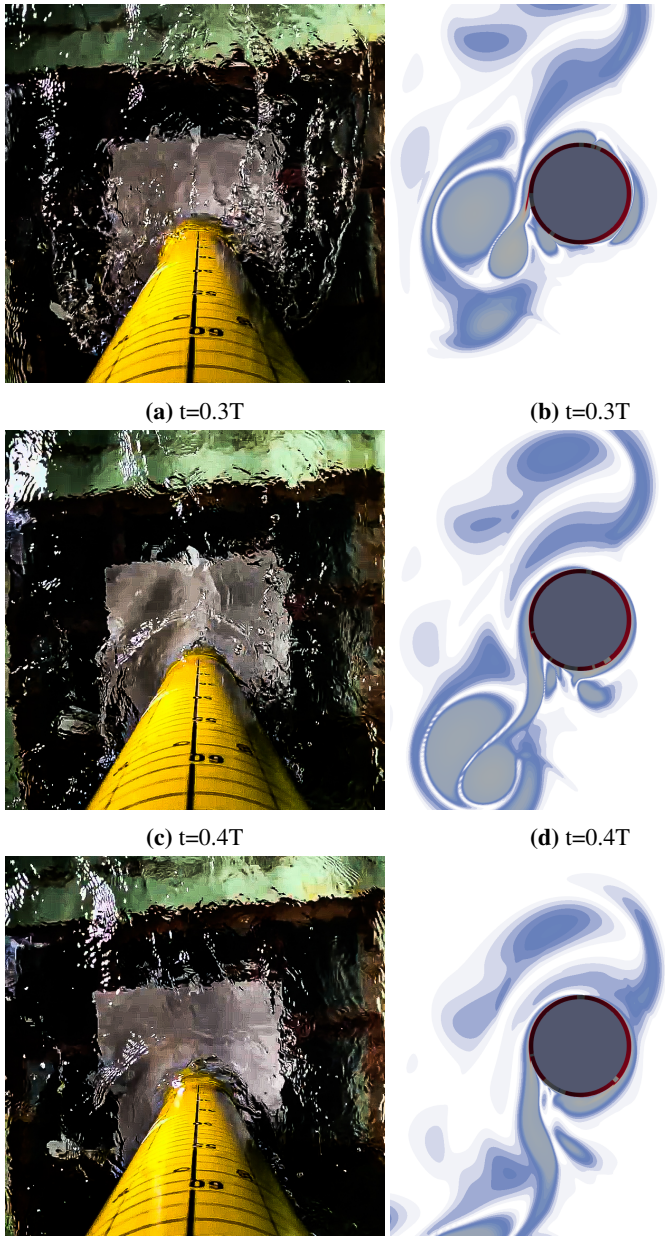

(a) t=0.3T **(b)** t=0.3T

(c) t=0.4T **(d)** t=0.4T

(e) t=0.5 **(f)** t=0.5T

Figure A.5.2: Visual comparison of experimental vs numerical flow field (vorticity) for T=2.165 s,$H_1/\lambda = 1/25$.

(a) t=0.6T

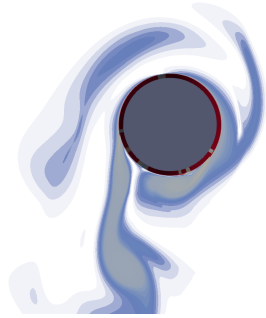

(b) t=0.6T

(c) t=0.7T

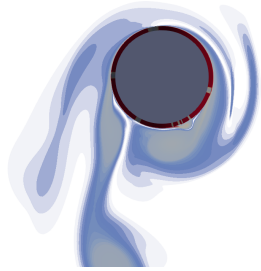

(d) t=0.7T

(e) t=0.8T

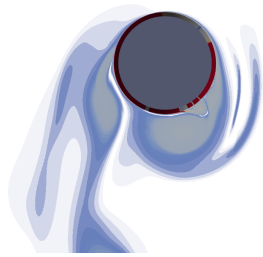

(f) t=0.8T

Figure A.5.3: Visual comparison of experimental vs numerical flow field (vorticity) for T=2.165 s,$H_1/\lambda = 1/25$.

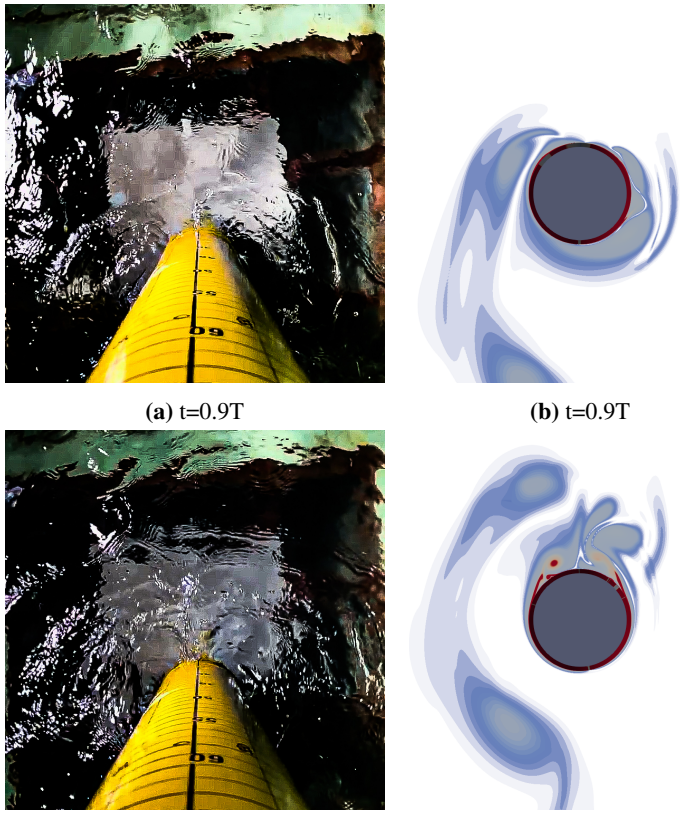

(a) t=0.9T **(b)** t=0.9T

(c) t=T **(d)** t=T

Figure A.5.4: Visual comparison of experimental vs numerical flow field (vorticity) for T=2.165 s,$H_1/\lambda = 1/25$.

A.6 3D discretisation

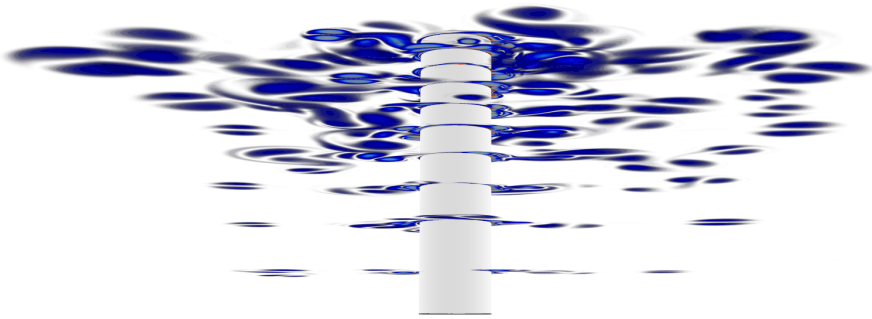

Figure A.6.1: 3D vorticity field below the wave crest for $H_1/\lambda = 1/25$ and T=1.73s, Seen from underneath

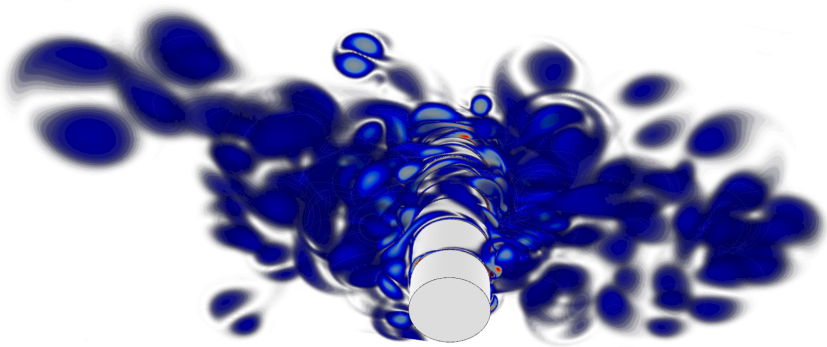

Figure A.6.2: 3D vorticity field below the wave crest for $H_1/\lambda = 1/25$ and T=1.73s, Seen from underneath

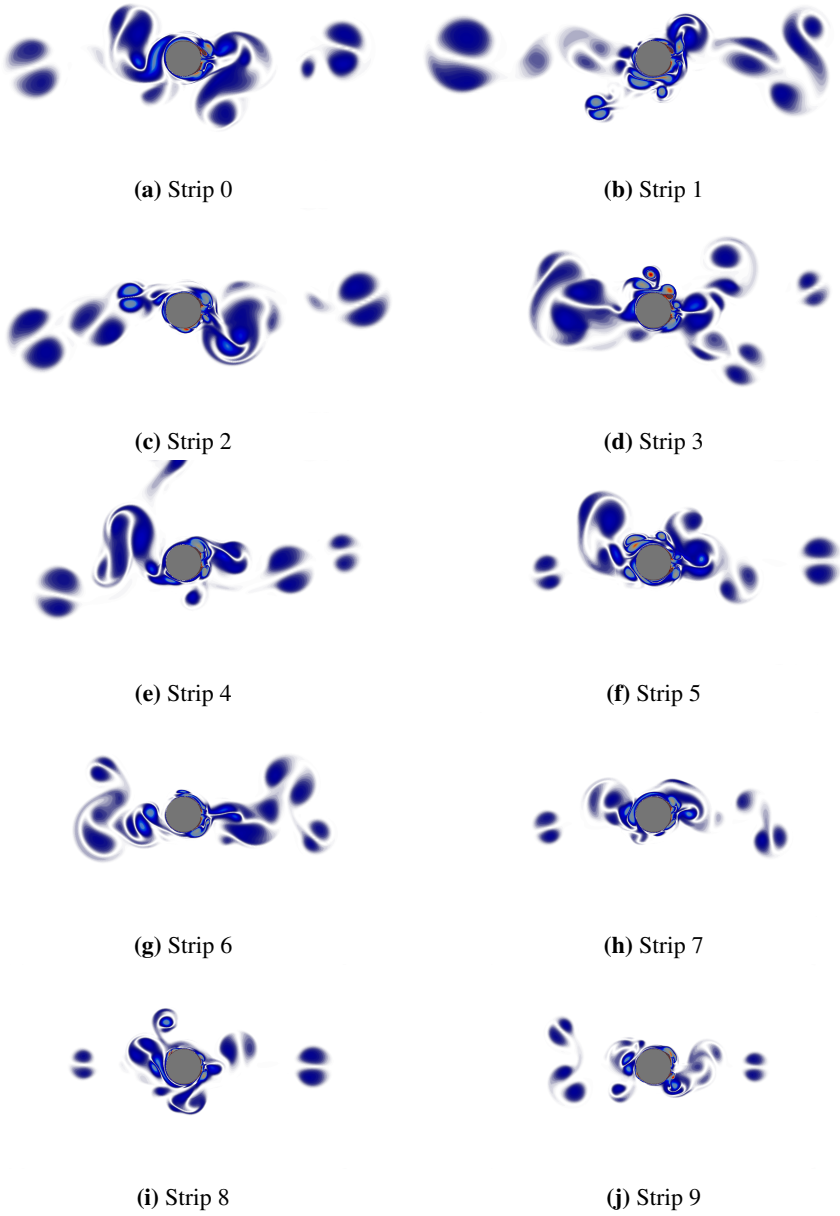

(a) Strip 0 **(b)** Strip 1

(c) Strip 2 **(d)** Strip 3

(e) Strip 4 **(f)** Strip 5

(g) Strip 6 **(h)** Strip 7

(i) Strip 8 **(j)** Strip 9

Figure A.6.3: Vorticity at the surface for $H_1/\lambda = 1/40$, T=1.73

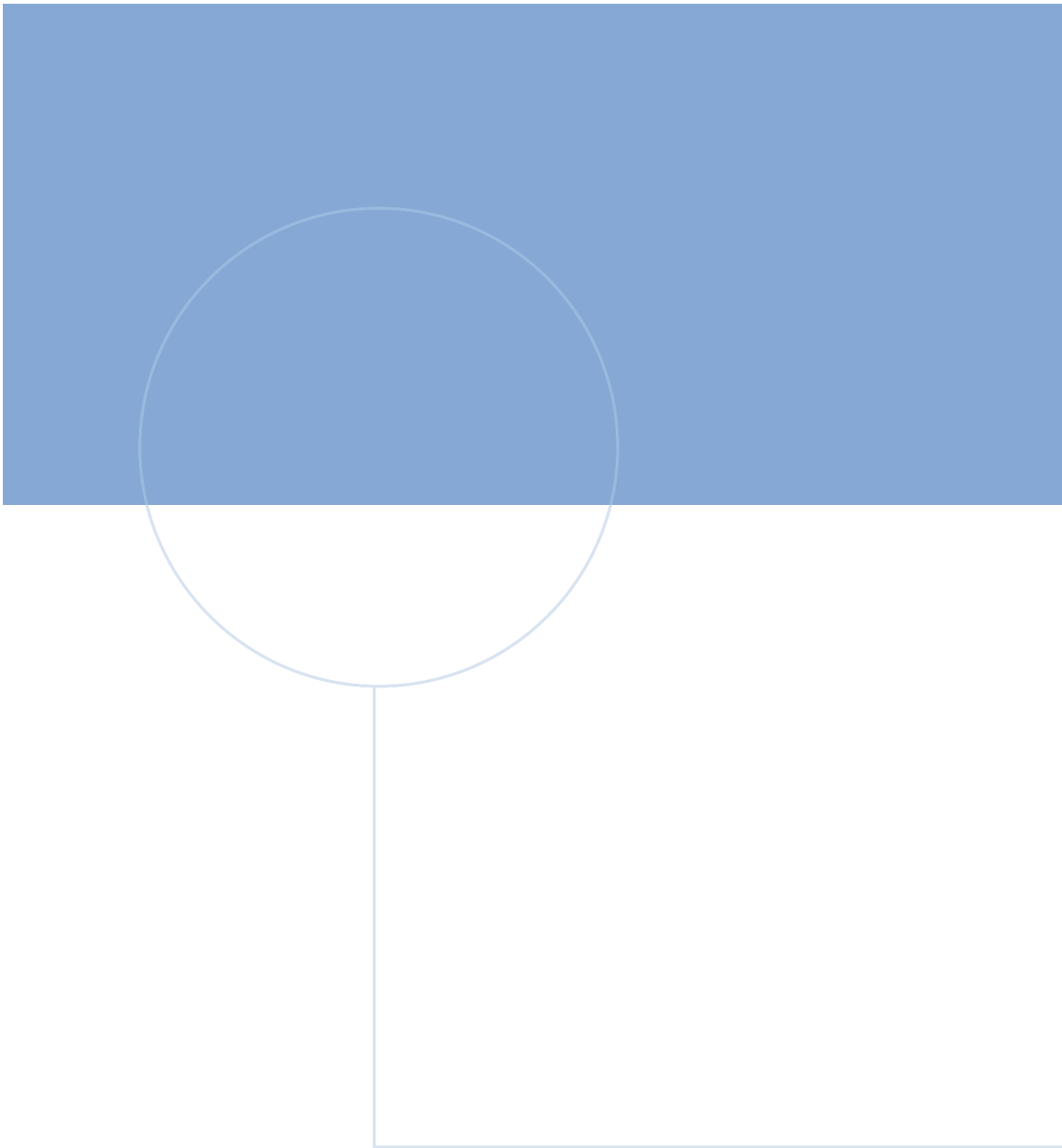

NTNU

Norwegian University of
Science and Technology